# Measurement of gravitational lensing of the cosmic microwave background using SPT-3G 2018 data

```
Z. Pano, 1,2,3,* F. Bianchinio, 4,5,6,† W. L. K. Wuo, 4,6 P. A. R. Ade, Z. Ahmed, 4,6 E. Anderes, A. J. Anderson, 9,2 B. Ansarinejad, M. Archipleyo, 11,12 K. Aylor, 13 L. Balkenholo, 10,14 P. S. Barry, R. Basu Thakur, 15 K. Benabed, A. N. Bendeo, 1,2,16 B. A. Benson, 9,2,16 L. E. Bleem, 1,2 F. R. Bouche, 14 L. Bryant, 17 K. Byrum, E. Camphuis, 14
A. N. Bender, "--" B. A. Bensor, "--" L. E. Bleem, "--" F. R. Bouchet, "4 L. Bryant," K. Byrum, E. Camphuis, J. E. Carlstrom, 17,3,1,16 F. W. Carter, T. W. Cecib, C. L. Chang, 2,16 P. Chaubal, G. Chen, P. M. Chichura, 2,2 H.-M. Cho, T.-L. Chou, 2,2 J.-F. Cliche, A. Coerver, T. M. Crawford, 2,16 A. Cukierman, 6,5 C. Daley, 11 T. de Haan, E. V. Denison, K. R. Dibert, 16,2 J. Ding, M. A. Dobbs, 19,24 A. Doussot, Dutcher, 3,2 W. Everett, C. Feng, K. R. Ferguson, K. R. Fichman, A. Foster, B. J. Fu, 11 S. Galli, A. E. Gambrer, R. W. Gardner, F. Ge, N. Goeckner-Wald, R. Gualtier, F. Guidi, S. Guns, N. Gupta, 10,29 N. W. Halverson, A. H. Harke-Hosemann, N. L. Harringtor, J. W. Henning, C. C. Hilton, E. Hivon, G. P. Holder, W. L. Holzapfer, J. C. Hood, D. Howe, N. Huang, K. D. Irwin, 5,6 O. Jeong, M. Jonas, A. Jones, F. Kéruzoe, T. S. Khaire, L. Knox, A. M. Kofman, 11,31 M. Korman, R. L. Kubik, S. Kublmann, C. J. Kup, 4,5,6 A. T. Legon, 20,32 F. M. Leitch, L. L. L. Legon, A. E. Lowitz, C. L. 126
N. Huang<sup>2,0</sup> K. D. Irwin,<sup>4,3,0</sup> O. Jeong<sup>6,0</sup> M. Jonas<sup>6</sup>, A. Jones<sup>6,0</sup> F. Kéruzoe<sup>6,1</sup> T. S. Khaire<sup>6,1</sup> L. Knox,<sup>1,3</sup> A. M. Kofman,<sup>1,3,1</sup> M. Korman,<sup>2,0</sup> D. L. Kubik<sup>9,0</sup> S. Kuhlmann<sup>1</sup>, C.-L. Kuo,<sup>4,5,6</sup> A. T. Lee<sup>2,0,3</sup> E. M. Leitch<sup>2,16</sup> K. Levy,<sup>10</sup> A. E. Lowitz<sup>2</sup>, C. Lu,<sup>26</sup> A. Maniyar,<sup>4,5,6</sup> F. Menanteau,<sup>1,12</sup> S. S. Meyer<sup>2,17,3,16</sup> D. Michalik,<sup>18</sup> M. Millea <sup>20</sup>, J. Montgomery<sup>1,0</sup> A. Nadolski,<sup>11</sup> Y. Nakato<sup>5</sup>, T. Natoli<sup>2</sup>, H. Nguyen<sup>9</sup>, G. I. Noble<sup>3,3,34</sup> V. Novosad<sup>3</sup>, Y. Omori<sup>2,16</sup> S. Padir<sup>2,15</sup> P. Paschos<sup>2</sup>, J. Pearson<sup>3</sup>, C. M. Posad<sup>2</sup>, K. Prabhu<sup>1,3</sup> W. Quan<sup>3,2</sup> S. Raghunathan<sup>12</sup> M. Rahimi,<sup>10</sup> A. Rahlin<sup>9,2</sup> C. L. Reichard<sup>10</sup>, D. Riebel<sup>1,8</sup> B. Riedel<sup>1,7</sup> J. E. Ruhl<sup>2,8</sup> J. T. Sayre<sup>2,5</sup> E. Schiappucci<sup>1,9</sup> E. Shirokoff<sup>2,16</sup> G. Smecher<sup>2,5</sup> J. A. Sobrin<sup>9,2</sup> A. A. Stark<sup>3,6</sup> J. Stephen<sup>1,7</sup> K. T. Story<sup>4,5</sup> A. Suzuki,<sup>32</sup> S. Takakura<sup>3,30</sup> C. Tandoi,<sup>1,1</sup> K. L. Thompson<sup>4,5,6</sup> B. Thorne,<sup>1,3</sup> C. Trendafilova<sup>1,4</sup> C. Tucke<sup>7</sup>, C. Umilta<sup>3,40</sup>, C. R. Vale<sup>2,2</sup> K. Vanderlinde<sup>3,3,34</sup> J. D. Vieira<sup>1,1,26,12</sup> G. Wang<sup>1</sup>, N. Whitehorn<sup>3,8</sup> V. Yefremenko<sup>1,1</sup> K. W. Yoon,<sup>4,5,6</sup> M. R. Yoong<sup>9,2</sup> and J. A. Zebrowski<sup>16,9</sup>
                                                                 <sup>1</sup>High-Energy Physics Division Argonne National Laboratory.
                                                                        9700 South Cass Avenue emont, Illinois 60439, USA
                                                              <sup>2</sup>Kavli Institute for CosmologicaPhysics,University of Chicago,
                                                                        5640 South Ellis AvenueChicago, Illinois 60637, USA
                          <sup>3</sup>Department of PhysicstJniversity of Chicago5640 South Ellis Avenu€hicago,Illinois 60637, USA
                                                  <sup>4</sup>Kavli Institute for Particle Astrophysics and Cosmolo@tanford University.
                                                                            452 Lomita Mall, Stanford, California 94305, USA
                            <sup>5</sup>Department ofPhysics,Stanford University382 Via Pueblo Mall,Stanford,California 94305,USA
                             <sup>6</sup>SLAC NationalAccelerator Laboratory 2575 Sand Hill Road, Menlo Park, California 94025, USA
                                      <sup>7</sup>Schoolof Physics and AstronomyCardiff University, Cardiff CF24 3YB, United Kingdom
                           <sup>8</sup>Department ofStatistics,University of California, One Shields Avenu@avis, California 95616,USA
                                    Fermi National Accelerator Laboratory MS209, P.O. Box 500, Batavia, Illinois 60510, USA
                                                <sup>10</sup>Schoolof Physics University of Melbourne, Parkville, Victoria 3010, Australia
                                                           <sup>1</sup>Department of Astronomy University of Illinois Urbana-Champaign.
                                                                         1002 WestGreen Street, Urbana, Illinois 61801, USA
                                           <sup>12</sup>Center for AstroPhysicaSurveysNational Center for Supercomputing Applications,
                                                                                                 Urbana, Illinois 61801, USA
                                                              <sup>13</sup>Department of Physics and Astronomy University of California,
                                                                            One Shields Avenu@avis, California 95616, USA
                                                <sup>14</sup>Institut d'Astrophysique de ParisUMR 7095, CNRS and Sorbonne Univereit
                                                                                98 bis boulevard Arago,75014 Paris, France
                           <sup>15</sup>California Institute of Technology, 1200 East California Boulevard., Pasadena, California 91125, USA
                                                           <sup>16</sup>Departmentof Astronomy and AstrophysickIniversity of Chicago,
                                                                        5640 South Ellis AvenueChicago, Illinois 60637, USA
                           <sup>17</sup>Enrico Fermi Institute, University of Chicago, 5640 South Ellis Avenue, Chicago, Illinois 60637, USA
                                                <sup>18</sup>University of Chicago, 5640 South Ellis Avenue Chicago, Illinois 60637, USA
                                                         <sup>19</sup>Departmentof Physics and McGillSpace InstituteMcGill University,
                                                                    3600 Rue UniversityMontreal, Quebec H3A 2T8Canada
                                            <sup>20</sup>Department of Physics, University of California, Berkeley, California 94720, USA
                                   <sup>21</sup>High Energy Accelerator Research Organization (KEK)sukuba Ibaraki 305-0801, Japan
                              <sup>22</sup>NIST Quantum Devices Grouß,25 Broadway Mailcode 817.03Boulder, Colorado 80305,USA
                                                                  <sup>23</sup>Materials Sciences DivisionArgonne NationalLaboratory,
                                                                        9700 South Cass Avenueemont, Illinois 60439, USA
                             <sup>24</sup>Canadian Institute for Advanced Resear@IFAR Program in Gravity and the Extreme Universe,
                                                                                         Toronto, Ontario M5G 1Z8, Canada
```

<sup>25</sup>CASA,Department of Astrophysical Planetary Science Iniversity of Colorado, Boulder, Colorado 80309, USA <sup>26</sup>Departmentof Physics,University of Illinois Urbana-Champaign, 1110 WestGreen Street Urbana, Illinois 61801, USA <sup>27</sup>Department of Physics and Astronomlyniversity of California,Los AngelesCalifornia 90095,USA <sup>28</sup>Departmentof Physics,Case Western Reserve Universityleveland,Ohio 44106,USA <sup>29</sup>CSIRO Space and AstronomPO Box 1130,Bentley,Western Australia 6102Australia <sup>30</sup>Departmentof Physics, University of Colorado, Boulder, Colorado 80309, USA <sup>31</sup>Departmentof Physics and AstronomyUniversity ofPennsylvania, 209 S.33rd Street, Philadelphia, Pennsylvania 19064 USA <sup>32</sup>Physics DivisionLawrence Berkeley Nationalaboratory, Berkeley, California 94720, USA <sup>33</sup>Dunlap Institute for Astronomy and Astrophysidsniversity of Toronto, 50 St. George Street, Toronto, Ontario M5S 3H4, Canada <sup>34</sup>David A. Dunlap Department Astronomy and Astrophysict Iniversity of Toronto, 50 St. George Street, Toronto, Ontario M5S 3H4, Canada <sup>35</sup>Three-Speed Logidnc., Victoria, British Columbia V8S 3Z5Canada 36Harvard-Smithsonian Center for Astrophysic Garden Street, Cambridge, Massachusetts 02138 ISA <sup>37</sup>Departmentof Astrophysicaland Planetary Sciences Iniversity of Colorado, Boulder, Colorado 80309, USA <sup>38</sup>Department of Physics and Astronomy, Michigan State University, East Lansing, Michigan 48824, USA

(Received 22 Augus 2023; accepted 31 October 2023; ublished 12 December 2023)

We present a measurement of gravitational lensing over 15000dlebge Southern sky using SPT-3G temperature data at 95 GHz and 150 GHz taken in 2018. The lensing amplitude relative to a fiducial Planck 2018 Lambda cold dark matter (ΛCDM) cosmology is found to be 1.020 0.060, excluding instrumental and astrophysicallystematic uncertaintie. We conductextensive systematic and nutlests to check the robustness of the lensing measurements, and report a minimum-variance combined lensing power spectrum over angular multipoles of 50 < L < 2000, which we use to constrain cosmological models. When analyzed alone and jointly with primary cosmic microwave background (CMB) spectra within the ΛCDM model, our lensing amplitude measurements are consistent measurements from SPT-SAPTpol, ACT, and Planck. Incorporating loose priors on the baryon density and otherparameters including uncertainties on a foreground bias template, we obtain a 1σ constraiթΩβΑ5σ4 0.595 0.026 using the SPT-3G 2018 lensing data alone, wheeeacommon measure of the amplitude of structure today and  $\Omega_{\rm m}$  is the matter density parameter. Combining SPT-3G 2018 lensing measurements with baryon acoustic oscillation (BAO) data, we derive parameter constraints of 0.031, 0.0330.836 0.039, and Hubble constant #1/4 68.8 1.3 km s<sup>-1</sup> Mpc<sup>-1</sup>. Our preferred Svalue is higher by 1.6 to 1.8σ compared to cosmic shear measurements from DES-Y3, HSC-Y3, and KiDS-1000 at lower redshift and smaller scales. We combine our lensing data with CMB anisotropy measurements from both SPT-3G and Planck to constrain extensions of ACDNUsing CMB anisotropy and lensing measurements from SPT-3G only, we provide independent constraints on the spatial curvatura of 01 40.023 (95% C.L.) and the dark energy density of  $\Omega$ 4 0.72 $2_{0.026}^{0.031}$  (68% C.L.). When combining SPT-3G lensing data with §PT-3G CMB anisotropy and BAO dataye find an upper limit on the sum of the neutrino masses of m<sub>v</sub> < 0.30 eV (95% C.L.). Due to the different combination of angular scales and sky area, this lensing analysis provides an independenteck on lensing measurements by ACT and Planck.

DOI: 10.1103/PhysRevD.108.122005

#### I. INTRODUCTION

are deflected by the intervening gravitational potentials of way to map the projected matter distribution of the

panz@anl.gov <sup>†</sup>fbianc@slac.stanford.edu

surface of last scattering e.g.,[1]. The distortion of the Photons from the cosmic microwave background (CMB) primordial CMB by gravitational lensing provides a unique the large-scale structure (LSS) as they travel to us from the CMB fluctuations on different angular scales. We can leverage these correlations to reconstruttle underlying projected matter over and underdensities and measure the CMB lensing potential power spectrum, from which we can infer the underlying matter power spectrum. Thanks to the rom weak lensing measurements from optical galaxy high redshift ( $z \approx 1100$ ) of the CMB, lensing measurements contain LSS information from the last scattering surface to the present day, with the maximum of the lensing ependent such as SPT-3GACT, and Planck, provide therefore probe the large-scale structure and can inform these tensions. many key topics in cosmology, including the amplitude of matter density fluctuations [2,3], the mass of the neutrinosused in this analysis in Sec. II and the simulations in [4–8], the nature of dark energy [9] and gravity [10–13].

several experiments, including ACT [3,14–16], BICEP/ Keck [17,18], Planck [19–22], POLARBEAR [23,24], and robustness of the results in the same sectidn. Sec. VI, SPT [25–30]. The tightest lensing amplitude measurements explore the cosmological mplications of our lensing currently come from the DR6 datasety Advanced ACT [ACT hereafter; 2.3%, [3]] and from Planck NPIPE maps isolation and then in combination with BAO and primary (2.4%, [22]).

This work presents the firstensing measurementom SPT-3G, the current camera on the South Pole Telescope, using data taken during the abbreviated 2018 season when

"" feet plans were fully In this section, we introduce the telescope and receiver operational.CMB primary anisotropy cosmology results from the SPT-3G 2018 data are published in Dutcher et al. map-level processing for this lensing analysis. [[31] hereafter D21] and Balkenhol et al. [32,33].

The focuses of this paper are lensing power spectrum measurements rom the SPT-3G 2018 data and their cosmological implications, though we also show the reconstructed lensing mapsCompared to previous SPT lensing measurementsur input maps have higher noise than those used in the SPTpol measurements presented inequency bands centered at 95 GHz, 150 GHz, and than the temperature-only SPT-SZ measurements in Omori6,000 detectors and arcminute angularesolution given lensing reconstruction and the resulting SPT-3G lensing map's S=N ratio per mode is lower than that from SPTpol and higher than that from SPT-SZ. However, because of the sky extending in right ascension from 20 40 m0s to larger area of SPT-3G compared to SPTpol and lower nois 100 and in declination from −42° to −70°. We divide compared to SPT-SZ, we are able to constrain the lensing his survey field into four subfields centered at-44.75°, amplitude with uncertainties similar to both previous measurements at ≃6%.

With this stringent lensing measurement he SPT-3G 2018 data already enables competitive constraints on cosmological parameters alone and in combination with external datasets in constraints are particularly interesting in light of the current tensions in cosmology, in which cosmological parameters inferred using different probes, each with high precision, do not agree with each other. Specifically, measurements of H<sub>0</sub> from the Cepheidcalibrated local distance ladder and the CMB from Planck are in tension at the  $5.7\sigma$  level [34–37]. Additionally, the structure growth parametes, inferred

surveys, shows a discrepancy with the value suggested by CMB data [38–40]. Experiments that are relatively kernel around redshift of 2. Lensing measurements can cross-checks, allowing for a more detailed investigation of

This paper is organized as follows. We describe the data Sec.III. We then summarize the lensing analysis steps in Lensing measurements have been made with data from Sec. IV. We present the lensing mappower spectraand amplitude parametersin Sec. V. We also discuss the measurements for the ACDM model and extensions, first in CMB data. We conclude in Sec.VII.

#### II. DATA

used to collect the raw data, the data reduction, and the

#### A. Instrument and CMB observations

The South Pole Telescope (SPT) is a 10-meter diameter submillimeter-quality telescope located at the geographical South Pole [41]. The currently operating third-generation receiver, SPT-3G [42], has polarization sensitivity and three Wu et al. [[28] hereafter W19] and cover a smaller patch 220 GHz. The combination of high sensitivity from about et al. [[27] hereafter O17]We use temperature data for thisthe 10-meter primary mirror makes the resulting maps an ideal dataset for CMB lensing analysis.

> The main SPT-3G survey field covers a 1500 obaqueh -52.25°, -59.75°, and -67.25° declination to minimize the change in optical loading and detector responsivity during the observation of any one subfield. The telescope observes using a raster scanning strategyhere it completes a left and right scan over the full azimuth range at constant elevation and then moves in elevation by approximately 12 arcmin until the full elevation range of the subfield is complete.

> We use data from the 2018 observing season forthis paper. During 2018, problems with the telescope drive system and receiver resulted in a half-season of observation with only 50% of the detectors operational. The remaining operable detectors had excess low frequency noise due to detector wafer temperature drifts, which can be filtered out during data processing. Subsequent epairs were undertaken during the 2018 Austral summer, successfully restoring instrumentperformance and observation efficiency to the anticipated level. We describe processing of althree

<sup>&</sup>lt;sup>1</sup>In [27], SPT-SZ and Planck maps are inverse-variance combined over the 2500 square degree SPT-SZ observing field before lensing reconstructionMost of the lensing S=N ratio comes from the SPT-SZ maps.

We do not include polarization data for the same reason. As no be statistically similar among themselves. we will show, the 2018 datasethas sufficient depth for competitive measurements | lensing and cosmological parameters.

# B. Time-ordered data to maps

We start with the time-ordered data (TOD) from the detectors and calibrate them using observations of two Galactic star-forming HII regions; RCW38 and MAT5a (NGC3576). To reduce the low-I noise from atmospheric fluctuations and detector wafer temperaturedrifts, we subtracta 19th-order Legendre polynomial and remove modes corresponding to multipoles ≤300 along the scan direction from the TOD for each constant-elevation scan. calculate the averaged signal across all detectors within the Additionally, we apply a common-mode filter where we same wafer and frequency band and subtract the averaged. signal from each detector's TOD for the corresponding detector group. The common-mode filter is more efficient apply a filter that passes frequencies corresponding to I < uting to the final map. 6000 to the TOD for individual scans to avoid aliasing of frequency of the two-arcminute map pixel. To avoid undesired oscillatory features when we fit polynomial or other filtering templates to the TOD around bright sources, we mask point sources matching one ormore 150 GHz, and 220 GHz in the TOD when constructing the information. Out of 602 subfield observations in 2018, filter templates for the above filters. The masks for all frequency bands are the same and contain talk sources mentioned above. This masking is applied to the TOD for inverse-variance weights to reduce the map noise. each detector, zero-weighting samples within a certain radius from the location of the point source while leaving other weights at unity. The TOD masking radius is Sfor sources with maximum flux across the frequency bands between 5 mJy and 20 mJy,50 for sources greatethan 20 mJy, and 5<sup>0</sup> for galaxy clusters. The point source regions, just as the rest of the TOD, have the filtering templates subtracted, and are then binned to maps. This different from the map-levelinpainting and masking discussed in SecII E.

After filtering, detector weights are calculated based on their noise in the frequency range corresponding to the angular multipole range of 300 < I < 2000 with our telescope scanning speedWe calculate the weights in

bands and use only data from 95 GHz and 150 GHz for multipole space instead of frequency space and with the cosmological inference since the 220 GHz channel is threlew side of the multipole range set lower compared to [31]. times noisier and the inclusion of data at 220 GHz does not bis effectively downweights observations with high low-l significantly improve the lensing reconstruction S=N ratio noise, allowing the noise properties for different observa-

We perform data quality checks and cut data on several levels: individual detectors in a single scan or allobservations, all data in a scan, and all data in a subfield observation.

Many cuts are done at the detector level. Data from a The data processing methods are similar to those in [3 detector is cut from a scan if there are sharp spikes in the with a few major differences. We summarize the steps and σου, oscillations from unstable bolometer operation, OD (one glitch over 20 $\sigma$  or more than seven glitches over anomalously low TOD variance, or response lessthan S=N ratio of 20 to a chopped thermal source during calibration. A detector is also cutif the bias point is not in the superconducting transition or if the readout is beyond its dynamic range. While the above reasons constitute most detector cuts, there are cuts due to technical reasons in data processing that cause a detector to have unphysical values or miss identifying information. We remove detectors with anomalously high or low weights beyond  $3\sigma$  of the mean čut one of ten detectorwafers because ofexcess noise power at 1.0 Hz, 1.4 Hz (pulse tube refrigerator frequency), at removing atmosphere noise correlated among the detectors, the other cuts discussed above removed ≈20% of 10 Hz, and their harmonics. Out of the remaining operable primarily addresses uncorrelated low-frequency noise. We will be a substantial with the substantial detectors which results in around 8340 detectors contrib-

Cuts are also done at the level of complete scans. All data high-frequency signal and noise beyond the spatial Nyquist survive the detector cuts or the telescope pointing range does not match the intended survey field's range.

> Additionally, cuts are done to entire observations at the level of subfields. We cut subfield observations without complete calibration information or detector mapping we retain 569 for a total of ~1420 observing hours.We coadd all observations corresponding to one subfield with

We convert TOD into maps with detector pointing information, detector weights, and detector polarization properties following the same procedure as discussed in [31]. We make maps in the oblique Lambert azimuthal equal-area projection first with square one-arcminute pixels to avoid aliasing. We then apply an antialiasing filter in Fourier space, which removes information beyond the Nyquist frequency corresponding to the map resolution, ănd average every four-pixel unit into one twoarcminute pixel.

#### C. Beam

We measure the telescope beam using a combination of Mars and pointsource observations ([31also similar to

Keisler et al. [43]). The Mars observations have high S=N ratio out to tens of arcminutes away from the peak response 10but show signs of detector nonlinearity near the peak. We therefore mask the data obtained during a scan around Mars within ≈1 beam full width at half maximum (FWHM). To  $[\mu {
m K}^2]$ fill the hole around the peak planetesponse (≈1 arcmin radius), we stitch the Mars beam with observations of fainter point sources convolved with the Mars disk. The planet disk and pixelwindow function are later corrected after the stitching to obtain the beam profile. The beam uncertainty and correlations across multipoles are estimated by varying the combinations of point sources and Mars observations used for estimating different angular scales of the beam while also changing the parameters used to stitch the two types of maps together. The beam profiles are usef. 1. Noise spectra of coadded temperature maps fothe to obtain the calibration factors.

# D. Temperature calibration

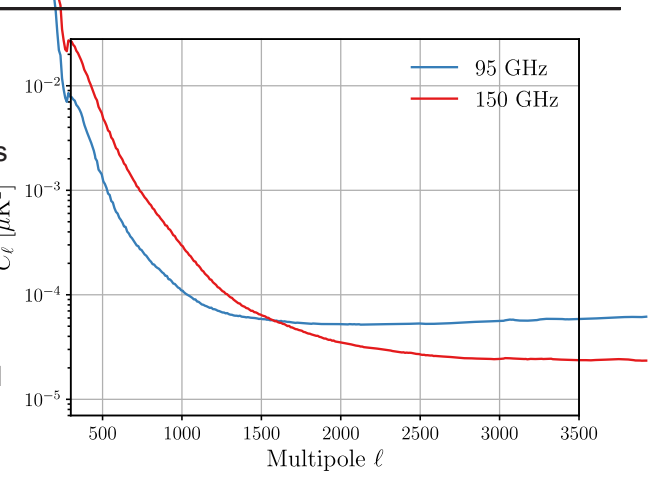
We obtain the absolute temperature calibration of the coadded maps by comparing the SPT-3G 95 and 150 GHwith samples drawn from a Gaussian random field with maps againsthe 100 GHz and 143 GHz maps from the Planck satellite (PR3 dataset) ver the angular multipole range of 400 < I < 1500. We compute the per-subfield calibration factor by dividing the SPT-3G cross-spectra between two half-depth SPT maps by the cross-spectra tion factors including the beam, pixel window function, and ollowing the shape of a cosine curve. Masking holes transfer function from map making applied (see Sec. III C)ntroduce a mean field that can be estimated using We mask brightpoint sources and galaxy clusters before ties of the per-subfield calibration factors are generated by ncertainties, we inpaint most of the sources and mask repeating the same analysis on 20 SPT-3G and Planck matching the original datasets (see also SedII C), and taking the standard deviation of the distribution for each subfield. The uncertainties are at the level of ≈0.3% and 0.2% for 95 and 150 GHz, respectively. We divide each subfield map by the corresponding calibration factor befor  $\mathbb{R}_1 < \mathbb{R} \le \mathbb{R}_2$ , where  $\mathbb{R}_1$  is the inpainting radius and  $\mathbb{R}_2$ stitching them to get the full 1500 degield map.

The noise spectra as a function of multipole, I, are plotted in Fig. 1. These curves are calibrated and corrected alizations for the transfer function and beam. Compared to 150 GHz. the 95 GHz data has less low-frequency noise from atmospheric fluctuations but higher noise at I > 1600. The resulting statistical uncertainty for the lensing spectra<sub>where 1</sub> indicates the R ≤ Region, 2 indicates the R<

is similar for 95 GHz and 150 GHz. The white noise levels  $R \le R_2$  region, T is the original map,  $\hat{T}$  is the inpainted are 26  $\mu$ K-arcmin and 17  $\mu$ K-arcmin for 95, and 150 GHz map,  $\tilde{T}$  is the simulated Gaussian map realization,  $\hat{Q}$  and at I ≈ 3000.

#### E. Source inpainting and masking

To mitigate the lensing biases from pointsources and



95 GHz and 150 GHz frequency bands.

combination of source inpainting and masking. The inpainting process replaces the pixels around the source power spectrum consistent with that of the CMB. The samples are constrained to have correlations with the surrounding pixels that follow the predicted CMB correlation function [44]. For source maskingwe multiply the map with a mask that effectively zeros the source pixels between full-depth SPT-3G and Planck maps, with correcasing cosine tapers, which smoothly decrease from 1 to 0, simulations and subtracted from the lensing map computing the cross-spectra to avoid biases. The uncertainty of the cross-spectra to avoid biases. The uncertainty of the cross-spectra to avoid biases. bright ones that are above 50 mJy at 150 GHz. Inpainting or simulation realizations, with power spectra and noise spectrasking sources and clusters with our thresholds discussed below corresponds to cutting 4% of the map area.

The inpainting method used here is similar to that used in Benoit-Lévy et al. [45] and [46]. We define two regions around the source or cluster center,  $R \le R_1$  and is fixed to be 25 We fill values within R based on values in the  $R_1 < R \le R_2$  annulus using constrained Gaussian

$$\hat{T}_1 \frac{1}{4} \tilde{T}_1 \triangleright \hat{C}_{12} \hat{C}_{22}^{-1} \delta T_2 - \tilde{T}_2 \triangleright;$$
  $\delta 1 \triangleright$ 

is the covariance matrix of the CMB fields between two regions X and Y. We generate Gaussian realizations in a fixed  $200^{\circ} \times 200^{\circ}$  box with the same CMB, foreground, noise spectra, and transfer function as the data to be galaxy clusters, we can remove them in map space using apainted. We estimate the covariance matrice \$\hat{\mathbf{c}}\_{12}\$ and C<sub>22</sub> with 5000 Gaussian realizations following the method in Benoit-Lévy et al. [46].

<sup>&</sup>lt;sup>2</sup>Planck Legacy Archivehttps://pla.esac.esa.int.

TABLE I. Inpainting and masking radii.

	Flux (S in mJy) or cluster S=N ratio	Inpainting radius	Masking radius
Point sources	S ≤ 6 6 < S ≤ 20 20 < S ≤ 50 50 < S ≤ 500	2 <sup>0</sup> 3 <sup>0</sup> 5 <sup>0</sup> 7 <sup>0</sup>	70
Galaxy clusters	S > 500 5 < S=N ≤ 9 S=N > 9	10 <sup>0</sup> 5 <sup>0</sup> 6 <sup>0</sup>	10 <sup>0</sup>

We inpaint or mask all sources detected above S=N rathe coordinates of pixel j. of 5 in any of the three frequency bands. The S=N ratio threshold roughly corresponds to minimum fluxes of 2.7 mJy, 3.3 mJy, and 12.0 mJy at 95 GHz, 150 GHz, and 220 GHz. We set the inpainting radii based on the source. The radii are summarized in Table I. We inpaint all the standard covariance matrix S ½  $^{\prime}$   $^{\prime}$   $^{\prime}$   $^{\prime}$   $^{\prime}$   $^{\prime}$ detected sources, including the brighter sources (>50 mJy) that will be later zeroed by masking to reduce the impact of noise.  $C_1^{TT}$  represents the sum of CMB and foretheir variance in the covariance matrix on neighboring regions to be inpainted. Similarly, we inpaint clusters detected with S=N ratio > 5. The cluster-finding process compared to the S=N ratio reported for the same clusters spectra representing tSZ, kSZ, CIB, and diffuse radio the SPT-SZ survey [47]. Note that this is a preliminary cluster list, and the S=N ratio for a full analysis will be much higher.

Table I). The source mask has cosine tapers with a radiusband. We solve for with a conjugate-gradient solver. 10°. With ~4% of the area lost due to masking and inpainting, we expect the bias from masking locations correlated with the underlying  $\phi$  field to be negligible (see e.g., [48]). The masking thresholds correspond to 361 sources being masked, and the resulting mean field is well atmospheric noise albw I, as well as astrophysical behaved. We show that the analysis is robust to these inpainting and masking choices in Set/. C.

30<sup>o</sup>-cosine taper to downweight the noisy field edges.

# F. Inverse-variance filtering

To minimize the variance of the reconstructed lensing map, the weights applied in the quadratic estimator include Sec. V C that our analysis is robust to different cut inverse-variance filtering the input CMB maps (Sec. IVA). choices. To construct the filter, we model the data maps as consisting of three components:the CMB sky signal, referred to as T<sub>I</sub>; "sky noise," N<sub>I</sub>, which includes astrophysical foregrounds and atmospheric noise; and pixel-domain noise,n<sub>i</sub>, modeled as white, uncorrelated,

and spatially nonvarying within the mask. We express the relationship between the data maps and the three components as follows:

$$X$$
  $X$   $X$   $Y_{jl}$   $Y_{jl}$   $Y_{l}$   $Y_{jl}$   $Y_{l}$   $Y_{l}$ 

Here, the matrix operator P<sub>il</sub> incorporates the transfer function and Fourier transform, enabling the conversion from Fourier space to map spacett is defined as Pil 1/4 eilx F, where F contains the beam, pixelization effects, and timestream filtering. The position vector represents

The inverse-variance filtered field is given by

ground spectra interpolated to 2D, while corresponds to the 2D anisotropic noise spectrum. The term n denotes the pixel-space noise variance multiplied by the mask. was performed using two years of SPT-3G data, resulting in For CITT, we use the same CMB and foreground spectra a S=N ratio for the detected clusters that is 1.5 times high amely a CMB TT spectrum and extragalactic foreground sources) that were used in generating the CMB simulations discussed in SecIII. To estimate C<sup>NN</sup>, we generate 500 noise realizations by subtracting the left-going and right-

In addition to the source inpainting, we apply a mask thating CMB maps and adding the difference maps with zeros the region around the brightest point sources in the random signs. We average the noise spectra over these 500 map. The masking radii are set by flux at 150 GHz for pointpise realizations and subtract a white noise level n, modeled sources and detection S=N ratio for galaxy clusters (see in pixel space, from the averaged 2D noise spectrum for each

#### G. Fourier space masking

In order to mitigate the contamination from instrumental foregrounds dominating over the CMB at high I, we apply a Fourier mask that includes modes in the multipole Besides source masking, we apply a boundary mask with ge of I between 300 and 3000 for the 95 GHz map and between 500 and 3000 for the 150 GHz map. In addition, we apply a cut excluding data with ≮ 300 and  $I_x < 500^3$  (referred as  $I_{min}$  cut hereafter) for the 95 GHz and 150 GHz frequency bands, respectively, to reduce some noisy modes along the scan direction below. I We show

<sup>&</sup>lt;sup>3</sup>Here I<sub>x</sub> refers to the axis along the x-direction in Fourier space after 2D Fourier transform of the map given the map projection we have chosen in Fig. 3, with x being the horizontal direction.

#### III. SIMULATIONS

response (normalization) and mean field correction to the foreground biases in SedV E. lensing map the lensing spectrum noise biases  $(N_1^1)$ , and biases to the lensing spectrum from extragalactic foregrounds.

# A. CMB and noise components

ogy from the bestfit of Planck 2018 TT,TE,EE+lowE +lensing [49]. We use CAMB [50] to generate CMB and lensing potential angular power spectra from the fiducial cosmology, and HEALPix [51] to synthesize spherical harmonic realizations of the unlensed CMB and lensing potential. We use Lenspix [52] to create lensed CMB realizations. The instrument and sky noise realization generation is described in Sed. F.

## B. Foreground components

The millimeter-wave sky, while dominated by the CMB at high galactic latitude, also contains signals from the cosmic infrared background (CIB), thermal and kinetic Sunyaev-Zel'dovich effects (tSZ, kSZ), and radio sources. We then mock-observe the simulations using the same We model the subinpainting-threshold/diffuse foreground by their measured angulapower spectra. The measured foreground spectra are based on Reichardt et al. [53] hereafterR21]. The CIB in the simulation consists of a Poisson-distributed component with D  $_{\rm L} \propto {\rm L}^{2}$  from faint dusty star-forming galaxies and a clustered part with  $D_1 \propto 1^{-0.8}$ . Here  $D_1$  is related to angular power spectrum  $C_1$  by  $D_1 \stackrel{1}{\cancel{4}} \frac{1}{2\pi} |\delta| \not = 1 \not = C_1$ . The spectral shape of the CIB is set to be  $v^{\beta}B_{v}\delta T_{dust}P$ , where  $B_{v}$  is the blackbody spectrum,  $T_{dust}$  is 25 K, and  $\beta$  is 1.48 for the Poisson term and 2.23 for the clustered term.At 150 GHz and I ¼ 3000, the amplitude of  $\mathbb{D}^{SIB}$  is  $D_{3000}^{CIB;P}$  ¼ 7.24  $\mu$ K² for the Poisson term and  $\frac{GB;cI}{5000}$  ¼ 4.03  $\mu$ K² for the clustered term. The clustered term includes the contributions from one- and two-halo terms [54]The shapes of the tSZ and kSZ angular power spectra follow the tSZ template in Shaw et al. [55] and the kSZ template in Shaw etal. [56] and Zahn et al. [57]. The amplitude at 143 GHz and I 1/4 3000 is  $D_{3000}^{tSZ}~1\!\!/_{2}~3.42~\mu\text{K}^{2}$  for tSZ and  $D_{3000}^{tSZ}~1\!\!/_{2}~3.0~\mu\text{K}^{2}$  for kSZ. The radio source component has a spectrum shape of  $D_1 \propto l^2$  and amplitude of  $\mathbb{Q}_{000}^{adio} \frac{1}{4} 1.01 \mu K^2$  at 150 GHz. measured values in [53] given the differentnasking and inpainting thresholds in this analysis described in Sec. II

We use these Gaussian foreground simulations to account for the contribution of foregrounds to the disconnected bias term (N <sup>0</sup>) in the lensing spectrum. However, this set of simulations does not account for

the nonzero trispectrum and primary and secondary bis-We use simulations to estimate the transfer function, the foregrounds. We discuss our approach to estimating the

Besides the diffuse foregrounds, the observed maps also contain point sources and galaxy clusters. We identify point sources and galaxy clusters in the data maps using simplified versions of methods in Everetet al. [60] and Bleem et al. [47]. We check thatthe point source fluxes We base the simulated CMB skies on a fiducial cosmoland the galaxy clusters' peak amplitudes are unbiased and accurate to within 10% based on previous measurements for overlapping detectionsWe include pointsources and clusters at their detected positions, amplitudes, and profiles in the simulated maps for all three frequencies. We use the beam profile for point sources and a beta profile [61] convolved with the beam for galaxy clusters. The point sources and clusters are the same between data and simulations, which allows us to use the same masks and inpainting for both.

# C. Simulation processing and transfer function

We convolve the simulated CMB and foreground maps with the corresponding beams of the three frequency bands. methods for data processing so thatthe mock-observed emissions below 6.4 mJy at 150 GHz as Gaussian described ulations have the same filter transfer function and mode coupling as the data maps We also add the noise maps discussed in SedJ F to the mock-observed maps.

> The transfer function is obtained as the square root of the ratio of the 2D power spectra of the mock-observed map and the noise-free simulated map. To reduce noise scatter in the estimate, we average and smooth the transfer functions obtained from 160 simulationsWe note thatthe transfer function shows a small dependence on the power spectra of the input maps. Small changes in the transfer function lead to variations in the weighting of the CMB modes at the inverse-variance filtering step (Sec. IIF), affecting the optimality of the filtered map. We show the effect of using different input spectra to estimate the transfer function on the reconstructedlensing spectra to be negligible in Sec. V C.

# D. Simulations for estimating foreground biases

While the simulations described so far are needed for pipeline checks and estimating the transfer function (Sec. III C) and lensing biases (Sec. IV Othey also assume no other astrophysical sources of statistical anisotropy besides lens-The population spectral index of the radio sources is set ting. However, extragalactic foregrounds are non-Gaussian be  $v^{-0.76}$ . The tSZ and radio spectra are adjusted from thethemselves and correlated with the lensing field. Therefore, we expect an extragalactic foreground bias to our measure-Ement. The galactic foregrounds have negligible effects on our lensing reconstruction since our field is chosen to have low galactic foregrounds.

To estimate the foreground bias, we use the AGORA simulation [59], an N-body-based simulation with tSZ, kSZ, CIB, radio sources and weak lensing components. A CMB map lensed with the  $\phi$  field obtained by ray-tracingeconstruction takesthe same form as the correlation through the lightcone is combined with appropriately scaled foreground components (thater correlated with φ) to produce mock 95 GHz and 150 GHz maps.

We create a parallelset of simulations with the same CMB field but Gaussian realizations of foregrounds that lations will later be used to estimate the foreground bias template in Sec. IV E. We have one full-sky realization of potential, and noise, AGORA simulations at 95 GHz and 150 GHz and we cut them into 16 patches the size of our observing field (Fig. 3). Theagora simulations, along with their Gaussian counterparts, undergo the same inpainting and masking procedure as the data described in Sed. E. This ensures that point sources and galaxy clusters have consistent masking threighependentand average to zeroso the averaged lensing of the inpainted and masked AGORA non-Gaussian simulations are within 10–20% of the simulations used for the from  $\phi_{\nu}^{T_{\nu}T_{\mu}}$ baseline analysis discussed in Sett.B.

#### IV. LENSING ANALYSIS

# A. Quadratic lensing estimator

The unlensed CMB is well-described by a statistically isotropic Gaussian random field with zero off-diagonal covariance Lensing breaks the statistical isotropy and introduces off-diagonaborrelations across CMB temperature and polarization modes in harmonic space the general case where X and Y ∈ ½T; E;tBe covariance in the flat-sky approximation is

$$hX_{l}\ Y_{l}\ _{0}i_{CMB}\ _{1}^{1/4}\ \delta\delta I-I\ _{0}^{0}D\zeta_{l}^{XY}\ b\ W_{l;l}^{XY}\ _{0}\varphi_{l-l}\ _{0}\ b\ O\delta\varphi^{2}b;\ \delta4b$$

where I (I <sup>0</sup>) is a vector in Fourier space, φ is the lensing potential, and CXY is the power spectrum of XYFor the temperature-based estimatore use in this paper, W is derived as the leading-order coefficient of the CMB correlation in terms of the lensing potential induced by lensing. In this work, we only include temperature erefore, in the remainder of the paper, we will replace X and Y with T  $_{v}$  and T  $_{u}$ , the temperature fields at frequencies v;  $\mu \in \frac{1}{2}95$ ; 150 GHz.

Using these off-diagonaborrelations, we can estimate weighted sum of the inverse-variance filtered lensing modes separated by L 1/4 I - I<sup>0</sup> [62]

Here we use an overbar to denote an inverse-varianceweighted quantity. W in Eq. (5) is designed to maximize the sensitivity to the lensing-induced signal while

minimizing noise. For temperature, WTT for lensing coefficient derived from Eq.(4).

In realistic cases,  $\overline{\varphi}_{l}^{\mathsf{T}_{\nu}\mathsf{T}_{\mu}}$  contains biases from other statistically anisotropic sources unrelated to lensisuch as the map mask and inhomogeneous sky noise. We estimate this map-level bias, which we call the mean field have identical power spectra to the sum of all non-Gaussian  $(MF) \stackrel{T_{\nu}T_{\mu};MF}{\phi_L}$ , by averaging the lensing estimations of 160 simulations with different realizations of CMB, lensing

The lensing potentials from different simulations are olds and corresponding radii as the data. The power specestimation only contains the MF from common nonlensing features shared among the simulations. We subtract the MF

> We normalize the mean-field-subtracted lensing potential by the inverse of the response. We obtain the total response by combining an analytic and a Monte-Carlo (MC) response estimate. The analytic response is given by

Here F  $_{l}^{T_{v}}T_{v;l}$  ¼ ½ $_{l}^{T_{c}}T_{v}^{T_{v}}$  þ N  $_{l}^{T_{v}}T_{v}^{T_{v}}$  is an approximation of the inverse-variance filtein Sec. II F, where the approximation is exactf there is no masking, and  $N_{\nu}^{T_{\nu}T_{\mu}}$ captures all anisotropic noise. For the general case, we apply an MC response correction, TRT,, MC to account for the deviation from this approximation. We divide the crossspectrum between the estimated lensing potentiald the input lensing potential by the input autospectrum and average this ratio over many simulation realizations to get the MC response

Here  $\varphi$  is the input lensing potential  $a\hat{\varphi}_{C}^{T/T_{\mu}}$  is the meanfield-subtracted lensing potential with analytic response the unnormalized lensing potential at L by calculating the normalization. We use a hat  $\hat{\phi}$  ) to denote debiased quantities. We also note that the response is the Fisher matrix for the lensing potential[19,26], making Eq. (5) an inversevariance-weighted quantity We average the MC response into 1D to reduce noise and get  $R_L^{T_vT_\mu;MC}$  1/4  $hR_L^{T_vT_\mu;MC}$  i. Here L is a vector in Fourier space, and hi means averaging over an annuli in 2D Fourier space corresponding to the same L. The MC response correction RT<sub>µ;MC</sub> is ≤10% across the range of scales used in this work.

The total responsecombining the analytic and MC response is  $R^{T_{\mu}} \frac{1}{4} R_L^{T_{\nu}T_{\mu};MC} R_L^{T_{\nu}T_{\mu};Analytic}$ , and the lensing potential estimate with the full correction is

$$\hat{\varphi}_{L}^{\mathsf{T}_{\mathsf{V}}\mathsf{T}_{\mathsf{\mu}}} \frac{1}{\mathsf{R}_{\mathsf{L}}^{\mathsf{T}_{\mathsf{V}}\mathsf{T}_{\mathsf{\mu}}}} \check{\mathsf{d}} \bar{\varphi}_{L}^{\mathsf{T}_{\mathsf{V}}\mathsf{T}_{\mathsf{\mu}}} - \bar{\varphi}_{L}^{\mathsf{T}_{\mathsf{V}}\mathsf{T}_{\mathsf{\mu}};\mathsf{MF}} \mathsf{P} \colon \qquad \qquad \mathsf{\tilde{0}} \mathsf{9} \mathsf{P}$$

# B. Lensing power spectrum, biases, and amplitude

We calculate the lensing power spectrum with the debiased lensing potentia  $\hat{\mathbf{g}}^{\mathsf{T}_{\nu}\mathsf{T}_{\mu}}$  and  $\hat{\boldsymbol{\phi}}^{\mathsf{T}_{\alpha}\mathsf{T}_{\beta}}$  from different frequency pairs. To account for the border apodization and where d denotes the data. In where d denotes the data. point source mask applied to the four temperature maps out a masking factor fask which is the average of the mask This method also suppresses off-diagonal tributions to applied to a single man to the fourth power from the the covariance of the lensing power spectrum [64]. applied to a single map to the fourth power, from the spectrum of the debiased lensing potential

The raw lensing power spectrum is biased by a few sources, including spurious correlations of the input fields to the zeroth and first order of the lensing spectrumant  $N_1^1$ , and the foreground bias to be discussed in Sec. IV E. There are higher-order biases in terms of the lensing spectrum such as the Ñ<sup>2</sup> biases from post-Born corrections and large-scale structure cross-bispectrathat are negligible given our noise levels [63]. The debiased lensing field. Here MC and MC<sup>0</sup> indicate that the simuspectrum after N and N<sup>1</sup> correction if spectrum after N and N1 correction is

$$\hat{C}_{I}^{\varphi\varphi} \frac{1}{4} C_{I}^{\hat{\varphi}\hat{\varphi}} - N_{I}^{RD;0} - N_{I}^{1};$$
 ő11Þ

where  $N_L^{\text{RD};0}$  is a variant of  $N_L^0$  to be introduced below. We estimate the Nand N bias terms with simulations. N<sub>1</sub><sup>0</sup> is estimated using

where  $C_L^{\hat{\varphi}\,\hat{\varphi}} \bar{\mathcal{T}}_\nu, \bar{T}_\mu, \bar{T}_\alpha, \bar{T}_\beta$  denotes the lensing crossspectrum between two debiased lensing potentials vT<sub>µ</sub> and  $\hat{\Phi}^{\mathsf{T}_{\alpha}\mathsf{T}_{\beta}}$ . We use this format instead of Eq. (10) to highlight the superscripts and subscripts when both are present.MC and MC 0 denote simulations with different realizations of the CMB, Gaussian foregroundlensing potential and noise. Applying Wick's theorem for the contraction in the above equation, only the Gaussian correlations between fields with the same superscript (MC or MC<sup>0</sup>) are nonzero. The N<sub>1</sub><sup>0</sup> estimated this way could be inaccurate because the data may have slightly different Gaussian power from the simulations depending on the simulation modeling and realization. To reduce the bias caused by the difference, we adopt a realizationdependent ND:0 [64] defined by

Spectra from lensing potentials estimated using both the data entering the quadratic lensing spectrum estimate, we divide simulation. We then subtraction to the subtraction of the subtracti

> The N<sup>1</sup> bias term arises from connected contributions to the trispectrum and is estimated using simulations with the same lensing field but different CMB realizations<sup>1</sup>. bias is given by

where  $\phi^1$  indicates that the simulations share the same realizations. The first two terms contain  $N_{L}^{0}$  bias from Gaussian power and the Nbias from the shared lensing potential among the four subfields. We subtract theias from the first two terms to get the N bias.

We presentour results in binned bandpowersOur bin edges are shown in Table II. We calculate the weighted average ofĈ<sub>i</sub><sup>φ</sup> within each bin,

TABLE II. MV lensing bandpowers.

1/2 min	L <sub>max</sub>	L <sub>b</sub>	10 <sup>7</sup> ½LðL þ 1βĈ <sub>L</sub> <sup>φφ</sup> =2π
1/250	67	59	0.958 0.336
1/268	91	80	1.261 0.233
1/292	125	109	1.061 0.164
½126	170	148	0.781 0.112
1/2171	232	202	0.636 0.081
1/2233	315	274	0.442 0.064
1/2316	429	373	0.356 0.044
1/2430	584	507	0.172 0.029
1/2585	794	690	0.084 0.022
1/2795	1080	938	0.061 0.018
1/21081	1470	1276	0.059 0.015
1⁄21471	1999	1735	0.021 0.013

MV lensing bandpowers as defined in Eq.17). Values are for

 $<sup>^4</sup>$ For clarity, here we suppress the frequency dependence of  $\frac{1}{2}$ LδL b  $\frac{1}{2}$ C $^{0}$ D and 2000. lensing reconstruction.

$$\hat{C}_{b}^{\varphi^{\mathsf{T}_{v}\mathsf{T}_{\mu}}\varphi^{\mathsf{T}_{\alpha}\mathsf{T}_{\beta}}} \equiv \frac{\mathsf{P}_{L \in \mathcal{P}_{L}^{\mathsf{T}_{v}\mathsf{T}_{\mu}\mathsf{T}_{\alpha}\mathsf{T}_{\beta}}} \hat{C}_{L}^{\varphi^{\mathsf{T}_{v}\mathsf{T}_{\mu}}\varphi^{\mathsf{T}_{\alpha}\mathsf{T}_{\beta}}} : \qquad \delta15\mathsf{P}$$

Here, the subscript b denotes a binned quantity. The weighted rainty. average of the Cinputs, denoted as Cis calculated using Wiener-filter weights w designed to maximize our sensitivity

D. Multifrequency lensing spectra combination to departures from the fiducial ΛCDM expectation;  $w_L^{T_vT_\mu,T_\alpha T_\beta}$   $\frac{1}{4}$   $C_L^{\varphi\varphi;theory}$ =Var $\hat{\mathbf{C}}_L^{\varphi^{T_vT_\mu\varphi^{T_\alpha T_\beta}}}$   $\triangleright$ . We obtain the variance Var $\hat{\mathbf{C}}_L^{\varphi\varphi}$   $\triangleright$  from analytic estimates of the signation where  $\mathbf{C}_L^{\varphi\varphi}$   $\triangleright$  from analytic estimates of the signation of the observed temperature fields at the (95, 95) GHz, (95, 150) GHz, noise spectrum.

 $A_h^{T_v T_{\mu}: T_{\alpha} T_{\beta}}$ , which is defined as the ratio of the unbiased lensing spectrum to the input theory spectrum:

$$A_b^{T_v T_\mu T_\alpha T_\beta} \equiv \frac{\hat{C}_b^{\varphi^{T_v T_\mu} \varphi^{T_\alpha T_\beta}}}{C_b^{\varphi \varphi; theory}} : \\ \hspace*{1.5cm} \check{\text{o}} 16 \text{P}$$

Here  $C_b^{\varphi\varphi;theory}$  is the theory power spectrum in bin b weighted the same way as in Eq. 15).

The overall lensing amplitude for each estimator is calculated in the same manners the per-bin amplitude in Eq. (16), using the entire range of reported L values.

#### C. Bias estimation using simulations

the following set of Gaussian simulations with inputs as detailed in Sec.III A and Sec. III B:

- A: 500 lensed simulations with foregrounds and noise realizations discussed in Self.F;
- set B, but different CMB.

We use all simulations in A to estimate  $\mathbb{N}^{0,0}$  and 340 lensing power spectrumWe use 160 simulations in A to calculate N1, which is proportional to the first order of lensing power and has no contribution from Gaussian foregrounds. The number of simulations used for each estimated term is chosen such that the term estimated lensing spectrum. In addition to these bias terms, simulations in A are used to estimate the transfer function (Sec. III C) and the covariance matrix for forming minimum-variancebandpowers(Sec. IV D). We have performed a pipeline test using Set A to confirm that the

We generate a set of 500 unlensed simulations using lensed CMB power spectrum and the same methods for on previous primary CMB SPT analyses [31,65] where the

foregrounds as in Set A. We use this set for various diagnostic tests, such as validating the mean lensing spectrum using this set of simulations being consistent with zero for each L bin within a fraction of the statistical

We can reconstruct three individual lensing potential temperature fields at the (95, 95) GHz, (95, 150) GHz, and (150, 150) GHz frequency combinations. By correlat-We can then compute the per-bin amplitude, denoted ang these three φ maps, we can extract a total of six separate lensing power spectra  $\mathfrak{P}$ .

> In this work, we combine the six individual debiased lensing spectra to produce a set of minimum-variance lensing band powers from temperature data-following previous analyses of primary CMB anisotropies, e.g., [[65,66], D21], we form a minimum-variance (MV) combination, in the frequency sense, of the lensing band powers £

Here, C is a vector of length 6N<sub>bins</sub> formed by concat-

$$C^{MV} /_{4} \delta X^{T} C^{-1} X P^{-1} X^{T} C^{-1} C$$
:  $\delta 17 P^{-1} X^{T} C^{-1} C$ 

enating the lensing power spectra extracted from the various frequency combinations, while C denotes their covariance matrix. X is a design matrix of shape 6N× To estimate the MF, Ŋ and Ŋ bias terms, we generate N<sub>bins</sub> in which each column is equal to 1 in the six elements corresponding to a lensing power spectrum measurement in that L-space bin and zero elsewhere. The band power covariance matrix C used to weight and combine the different lensing reconstructions is estimated with a sim-B: 160 lensed simulations with no foregrounds or noiseulation-based approach, using N sims 1/4 340 realizations C: 160 lensed simulations with no foregrounds or noiseintroduced in Sec.III. Given the finite number of simuand with the same realizations of lensing potential asations, the estimate of the covariance is noisy. To ameliorate the noise of off-diagonalelements, we condition the underlying covariance matrices by explicitly setting simulations in A to evaluate the statistical uncertainty of the zero those entries that we do not expect to be correlated. Specifically, we discard elements that are more than one bin estimate the MF (Sec. IVA), with 80 sims for each of the two lensing potential estimations that form the lensing spectrum. All of the simulations in set B and C are used to be be simulated by which is proportional to the first order of the simulations are correlated on average at the 15% level and no more than 30% inally, we note that the average correlation coefficient between different lensing reconstructions can be as large as 95% over the L range used in this analysis fortwo sets of lensing band converges well below the statistical uncertainty level of the powers that share three common frequencies, e.g.,  $\hat{C}_b^{\varphi^{T_95^T95}\varphi^{T_95^T95}} \text{ and } \hat{C}_b^{\varphi^{T_{95}^T95}\varphi^{T_{95}^T150}} \text{ and as low as } 56\% \text{ for } \hat{C}_b^{\varphi^{T_{95}^T95}\varphi^{T_{95}^T95}} \text{ and } \hat{C}_b^{\varphi^{T_{150}^T150}\varphi^{T_{150}^T150}}. \text{ We verified that the }$ conditioning applied to the cross-frequency covariance matrices results in a stable estimate of the MV lensing reconstructed lensing spectrum is unbiased compared to the true and its associated covariance matrix. Specifically, input lensing spectrum used to generate the simulations. we have tested two additionationditioning schemesone where we only retain the diagonal elements and one based

on- and off-diagonalcovariance blocks are treated differently, and found the differences in the recovered MV lensing spectra to be largely subdominant with respect statistical uncertainties.

# E. Astrophysical foreground bias template

We expect the lensing spectrum in Eq(11) to contain residual biases from extragalactic foregrounds. To address this, we estimate an extragalactic foreground bias template using the simulations described in Seld. D. We use this foreground bias template to model the shape of the bias spectrum and marginalize over its amplitude in our lensing amplitude measurement and when estimating cosmological parameters (Sed/I A 1).

To compute this template, we difference the lensing spectra extracted using the AGORA simulations with the lensing spectra from Gaussian realizations of foregrounds map,  $\hat{\varphi}^{T_{95}T_{150}}$  as representative noise levels e shown in black that have the same powerspectra as theimon-Gaussian foreground counterparts. The foreground bias template ( $T^m$ )ean field (MF) for  $\hat{\phi}^{T_{95}T_{150}}$  is plotted in dash-dotted lineThe can be expressed schematically as

$$\text{T } ^{1\!\!/4} \hat{C}_L^{\varphi\varphi} \delta \text{CMB}^{NG} \, \text{pFG} \, ^{NG} \text{p} - \hat{C}_L^{\varphi\varphi} \delta \text{CMB}^{NG} \, \text{pFG} \, ^G \text{p} \colon \ \, \delta 18 \text{p}$$

Here the superscripNG denotes the non-Gaussian simulations, and G denotes random Gaussian realizations with the same power spectrum. CMB dicates that the CMB is lensed by large-scale structures correlated with the foregrounds ( $F\mathfrak{G}^{IG}$ ) generated using the same set N-body simulations.The first term,  $\hat{C}_L^{\varphi\varphi}$   $\delta$ CMB $^{NG}$   $\flat$  FG $^{NG}$  $\flat$ , contains both the trispectrum of the foreground components the bispectrum with two powers of foreground and one trispectrum- and bispectrum-type biases have applied similar MF, response, and Ntorrections Eqs. (9) and (11) apply the  $N^1$  correction as it differences out Eq. (18). In addition to Eq. (18), we also estimate the foreground trispectrum and the bispectrum biasesseparately using  $\begin{array}{ll} \hat{C}_{L}^{\varphi\varphi} \delta CMB^{NG;2} \, \varphi \, FG^{NG} \flat \, - \hat{C}_{L}^{\varphi\varphi} \delta CMB^{NG;2} \, \varphi \, FG^{G} \flat & \text{and} \\ \hat{C}_{L}^{\varphi\varphi} \delta CMB^{NG} \, \varphi \, FG^{NG} \flat \, - \hat{C}_{L}^{\varphi\varphi} \delta CMB^{NG;2} \, \varphi \, FG^{NG} \flat, \text{check-} \\ \end{array}$ ing and confirming that their sum is consistentwith our indicates that the CMB comes from a different patch such convergence maplensing power spectrum, and lensing

combination (see Sec. IV  $\bar{D}$ ), as well  ${}^{RD}_{i}N_{i}N_{i}^{1}$ , and MF biases for  $\hat{\Phi}^{\mathsf{T}_{95}\mathsf{T}_{150}}$ . The  $1\sigma$  and  $2\sigma$  errorbars to the foreground template are estimated from the distribution of 16 bias power spectra estimated using Eq(18) for the 16 patches discussed in Sec. III D. We bin the MV foreground bias template using Eq.(15) to get the binned template  $C_h^{\varphi\varphi;fg}$ . The mean foreground bias amplitude is negative reconstructed from the individual frequency combinations

foreground or contribute to the bispectrum-type bias.

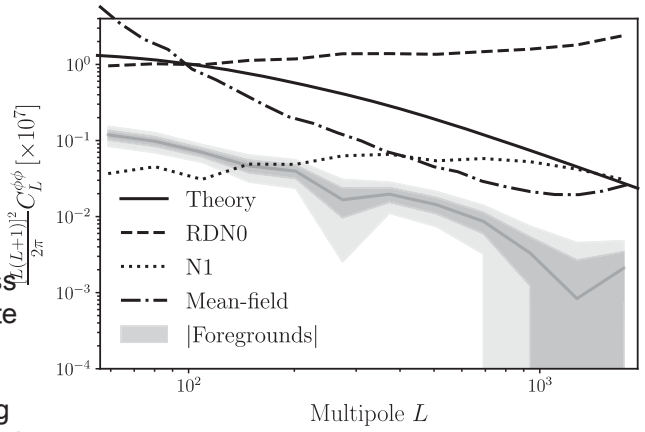


FIG. 2. Biases in the CMB lensing autospectrumThe solid black line denotes the fiducial CMB lensing power spectrum. The realization dependent Nand N1 biases for our deepest lensing dashed and dotted lines, respectively. The power spectrum of the absolute value of the expected mean foreground contamination to the minimum-variance combination (see SecIV D, negative bias) is shown by the solid gray line while the shaded gray areas denote the  $1\sigma$  and  $2\sigma$  scattewith respect to the mean calculated over 16 cutouts from the GORA simulations.

since the bispectrum-type bias is negativelativer L and larger in amplitude than the positive trispectrum-type bias term in the L range shown [59]. The bias amplitude reduces by ≈30% as we exclude modes with I > 2500, which is consistent with the foreground power becoming smaller Telative to the CMB atlower I.

As discussed in Sec. IV D, we combine the multifrequency power of the φ field. The second term contains neither, sqnformation in debiased lensing power spectrum spæse, their difference is an estimate of the sum of the foreground posed to lensing map space. Therefore, in Fig. 2, we show the mean field spectrum, N and N noise curves for the autospectrum ofô<sup>T95T150</sup>, our deepestlensing map, as a described in Sec. IV B for both lensing spectra. We do not representative noise level. The mean field spectrum at low L comes from the boundary mask and converges sufficiently with the number of simulations we used for averaging.

# V. LENSING MAPS, POWER SPECTRA, AND AMPLITUDES

template constructed using Eq. (18). Here the superscript 2 In this section, we present our main results: the lensing that its lensing field does not correlate with the non-Gaussamplitude measurement. We discuss the relative weights from independent frequency combinations and compare Figure 2 shows the foreground bias template to the MVour results to previous measurements by SPT-SZ (O17), SPTpol (W19), POLARBEAR [24], BICEP/Keck [18], Planck [22], and ACT [3]. We then discuss the lensing amplitude and its statistical and systematic uncertainties.

#### A. Lensing maps

In Fig. 3, we show the lensing convergence maps κ

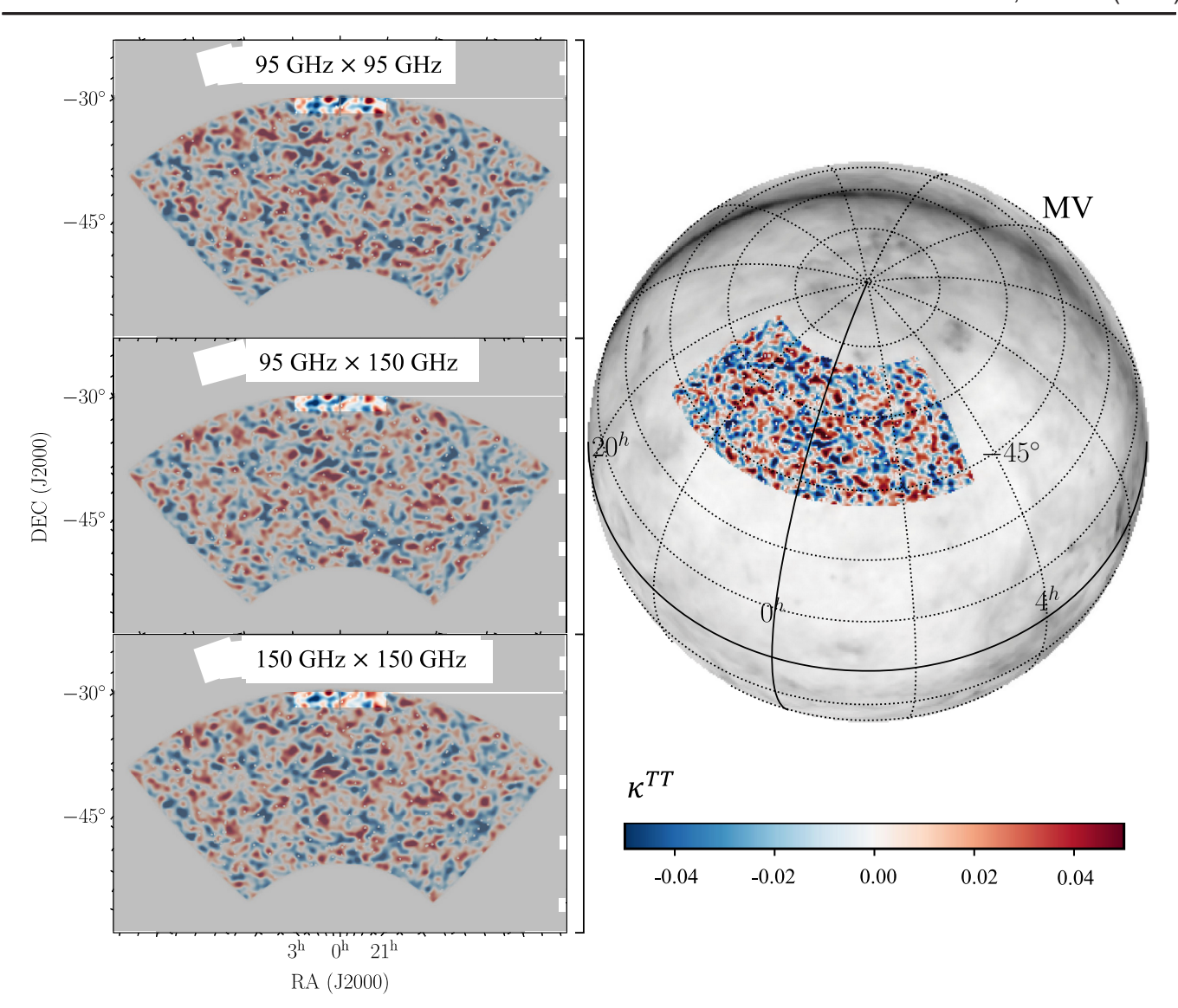


FIG. 3. Lensing κ maps reconstructed from the SPT-3G 150θ folded data, smoothed by a 1-degree FWHM Gaussian to highlight the large-scale modes with higher S=N rational have also multiplied the maps by the poisource and cluster mask discussed in Sec. II E. The three left panels show the lensing convergence map inferred from three independent requency combinations; 95 × 95 GHz, 95 × 150 GHz, and 150 × 150 GHz. The right-hand side shows a minimum-variance-combined CMB lensing convergence map reconstructed in this work using 95 GHz and 150 GHz data and projected to equatorial coordinates. The SPT-3G footprint covers approximately 1500 degree the southern sky. The background shows the Galactic durstap from Planck Commander in intensity plotted in a logarithmic color scale.

95 × 95 GHz, 95 × 150 GHz, and 150 × 150 GHz. The convergenceis related to the lensing potential  $\varphi$  as  $\kappa$  ½  $-\frac{1}{2}\nabla^2\varphi$ , which in harmonic space translates to  $\kappa_L$  ½  $\frac{L\delta L p_1 p}{2}\varphi_L$ . The  $\kappa$  maps in Fig.3 are smoothed using a 1-degree FWHM Gaussian filter to emphasize the large scale modes with higher S=N ratiour lensing maps are signal dominated atensing multipoles below L  $\approx$  7090, 100 for  $\hat{\varphi}^{T_{95}T_{95}},\; \hat{\varphi}^{T_{150}T_{150}},\;$  and  $\hat{\varphi}^{T_{95}T_{150}},\;$  respectively.The three panels on the left of Fig. 3 have nearly identical structures and are strongly correlat  $\hat{\varphi}^{T_{95}T_{95}},\; \hat{\varphi}^{T_{95}T_{150}},\;$  and  $\hat{\varphi}^{T_{150}T_{150}}$  share similar  $N_1^0$  noise contributions from

Gaussian power of the CMBthus their MV combination only slightly reduces the uncertainty compared to each individual frequency combination. We include the MV-combined lensing map on the right Fig. 3, which has almost the same structure as the panels on the left. We show the MV lensing map in equatorial coordinates to highlight the observing field for this analysis. Our lensing map covers three times the area and has higher reconstruction noise per mode compared to SPTpol (W19). On the other hand, our lensing map is 60% in size and has lower noise per mode compared to SPT-SZ (O17)Our lensing convergence maps show consistent degree-scalestructure

compared to both the SPTpoand SPT-SZ lensing maps visually.

# B. Lensing power spectra and amplitude

The lensing band powers from the six individual debiased lensing spectra and their MV combination, defined in Eqs. (16) and (17), are presented in Fig4. In addition, we have corrected for the foreground bias contamination estimated in Set E using AGORA simulations that closely match our observing frequencies and map processing steps. The foreground bias template is subject to uncertainties from sample variance and depen on the accuracy of the associated simulations. As a result ensing amplitudes foindividual frequency combinations and for cosmologicalinterpretation, but marginalize overthe amplitude of the foreground bias template  $A_{fg}$  with a conservative uniform prioras discussed in greater detail in Sec. VI A 1. We report the lensing power spectra in logarithmically spaced L bins between 50 and 2000he corresponding MV bandpowers and uncertainties are provided in Table II. The uncertainties of the individual bandpowersand the MV are similar because they are dominated by N, which is largely shared between lensing map reconstructed from the 95 GHz and 150 GHz input maps. In each multipole bin, the observed lensing power differs no more than ≤1σ between different reconstructions. The visual agreementacross the spectra recovered from different frequency combinations provides a consissubstantially larger in any one combination though more substantialtests will be done in the next section.

and their MV combination, defined also in Eqs.(16) and (17), in Table III. Similar to the bandpowerswe apply a

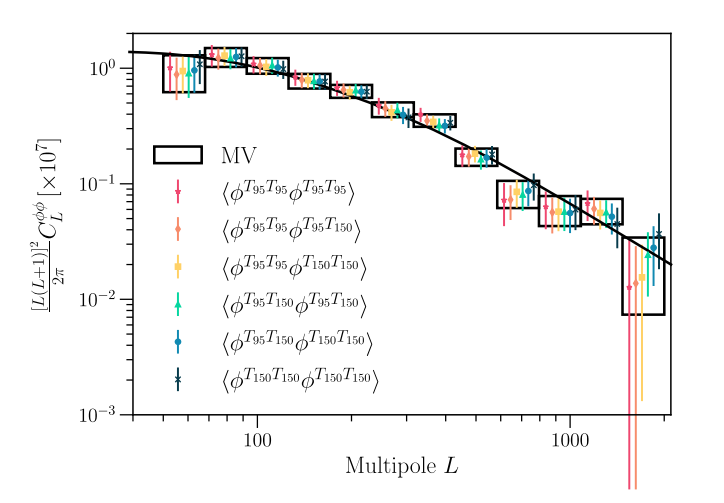


FIG. 4. Comparison of the MV lensing band powers reconstructed using temperature data at 95 GHz and 150 GHz (black boxes) againsband powers from individual frequency combinations (colored points) The solid line is the lensing spectrum from the Planck 2018 best-fit\CDM model.

TABLE III. Lensing amplitudes and uncertainties.

Frequency combinations	Amplitude	Statistical uncertainty	Systematic uncertainty
$\hat{C}_{l}^{\varphi^{T_{95}T_{95}}\varphi^{T_{95}T_{95}}}$	1.085	0.073	0.023
$\hat{C}_{1}^{\Phi^{T_{95}T_{95}}\Phi^{T_{95}T_{150}}}$	1.018	0.063	0.020
$\hat{\mathbf{C}}_{\mathbf{I}}^{\Phi^{T}_{95}T_{95}}\Phi^{T}_{150}T_{150}$	1.013	0.060	0.018
$\hat{\mathbf{C}}_{\mathbf{I}}^{\Phi^{T_{95}T_{150}}\Phi^{T_{95}T_{150}}}$	1.001	0.061	0.018
$\hat{\mathbf{C}}_{\mathbf{I}}^{\Phi^{T}_{95}T_{150}\Phi^{T}_{150}T_{150}}$	0.983	0.062	0.017
$\hat{\mathbf{C}}^{\Phi^{T}_{150}}_{\mathbf{T}}^{T}_{150}$	1.003	0.066	0.017
MV combined	1.020	0.060	0.016

we do not directly use these foreground-corrected spectratheir MV combination. The statistical and systematic uncertainties are also included. The total systematic uncertainties are evaluated by taking the quadrature sum of the individual contributions.

> foreground bias correction assuming the foreground template to be exact. To determine the statistical uncertainties. we utilize the standard deviation of the lensing amplitude distribution based on the 340 simulations within set A discussed in Sec. IV C. Our lensing amplitude for the MV combination is

Considering solely statistical uncertainty, the lensing amplitude for the MV combination is measured with an uncertainty of 5.9%, which is comparable to the uncertainties of tency check and suggests that the foreground biases are 60% using 95 GHz alone and 6.6% for 150 GHz alone. The uncertainty on the amplitude of  $\hat{C}_L^{\varphi^T_{95} \uparrow^T_{150} \uparrow_{150}}$  is the smallest among the six combinations because noncommon We summarize the lensing amplitudes for each estimat fluctuations (e.g., instrumental noise) between the 95 GHz and 150 GHz maps do not contribute to its in this case. We quantify the systematic uncertainties associated with the map calibration factor and beam uncertaining, Sec. V D. The systematic uncertainty for the MV combination lensing amplitude is 0.016, a fraction of the statistical uncertainties. Considering both statistical and systematic uncertainties, the measurement of the MV lensing amplitude has an uncertainty of 7.5%. In Sec. VI D 1, we also explore the lensing amplitude using a loose prior on the foreground bias template amplitude, Aand derive a constraint on the lensing amplitude of  $\mathbb{A}^{\phi}$  1/4 1.063 0.090. This result is consistent with the result reported in Eq. (19).

In Fig. 5, we compare our MV lensing spectra with other experiments. Our measurements agree with previous measurementsfrom SPT-SZ (O17), SPTpol (W19), Planck [22], and ACT [3]. We constrain the lensing amplitude at 5.9%, comparable to SPTpol 's 6.1% (W19) and SPT-SZ 's 6.3% (O17).

#### C. Consistency and null tests

To ensure the robustness of our analysis and identify potential systematic errors in the data, we conduct a suite of

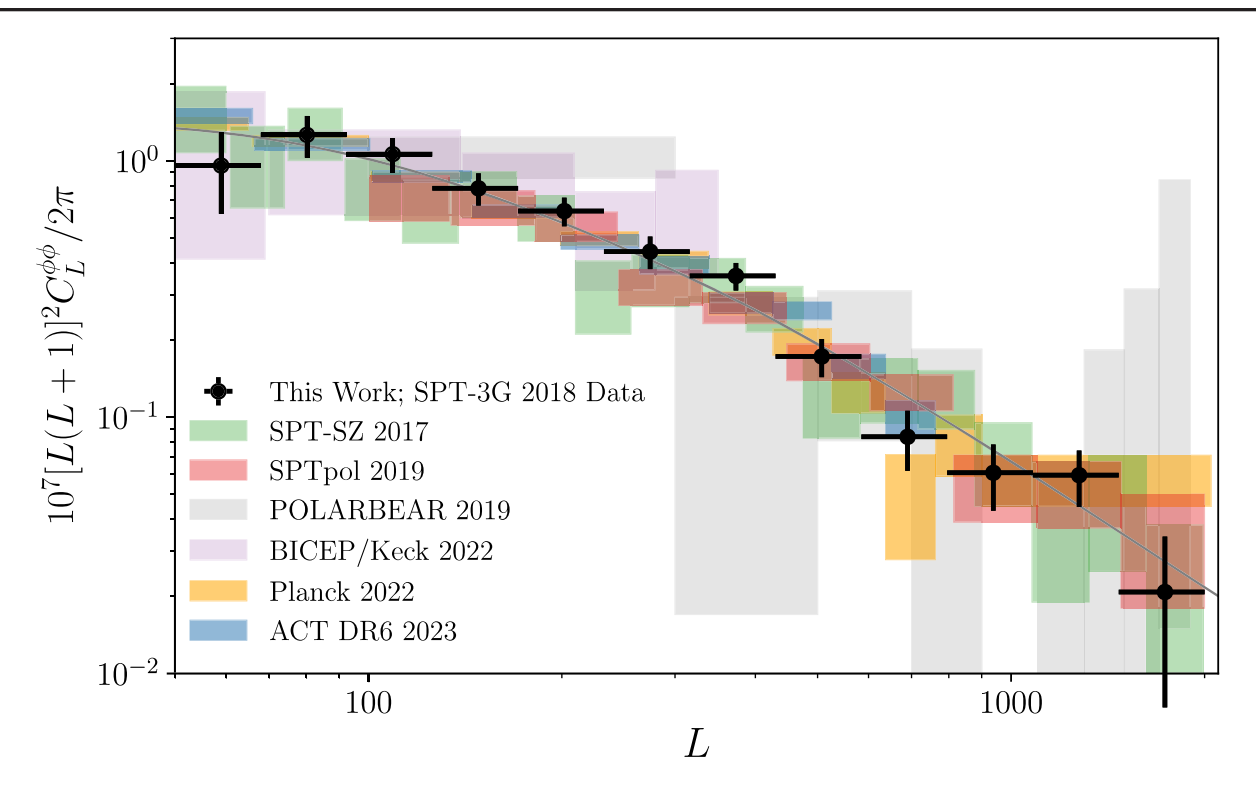


FIG. 5. Lensing power spectrum measurements from this workT-SZ (O17)SPTpol (W19),POLARBEAR [24], BICEP/Keck [18], Planck [22], and ACT [3]. We also plot the lensing spectrum from the best-fit CDM model to the 2018 Planck TT,TE, EE+lowE+lensing dataset (solid gray line) [34,49].

tests. For each testwe modify one aspect of the analysis our 340 simulations by replacing  $\hat{\mathbf{L}}_{b;data}$  with individual and recalculate the lensing power spectrum. We then assemulation spectra differencesThe probability-to-exceed the consistency of the results by comparing the bandpowepTE) is calculated as the fraction of simulation values obtained from the modified analysis with that obtained that are higher than the walue obtained from the data. We from the baseline analysis. The bandpowers obtained from ummarize the data  $\hat{\chi}$  and PTE results in Table IV. To the different analysis options are summarized in Fig. 6. We account for the look-elsewhere effect using the Bonferroni designed a suite of tests to specifically check the lensing

2.0

reconstruction and confirm the pipeline's robustness against unmodeled nonidealities in the data.

We quantify the  $\chi^2$  of the tests by comparing the difference data bandpower with the mean of the difference over 340 simulations (SeA in Sec. IV C), and using the variance of the per-bin simulation-difference spectrum to approximate the covariance diagonal, while neglecting the off-diagonal components, since the difference bandpowers. are largely uncorrelated across different bins. The the systematic tests are

$$\chi^2_{\text{sys}} \frac{1}{4} \frac{X}{b} = \frac{\delta \Delta \hat{C}_{b;data}^{\varphi \varphi} - h \Delta \hat{C}_{b;sim}^{\varphi \varphi} i b^2}{\sigma^2_{b;sys}}$$
:  $\delta 20b$ 

Here  $h\hat{\Omega}_{b;sim}^{\varphi\varphi}$  and  $\sigma_{b;sys}$  are estimated by performing the same analysis on the 340 simulations as on the data compute the differences in overall lensing amplitude. AA subtracting the two amplitudes and quantifying thesing the distribution of amplitude differences forthe simulations. We also use Eq. (20) to calculate theatues for all

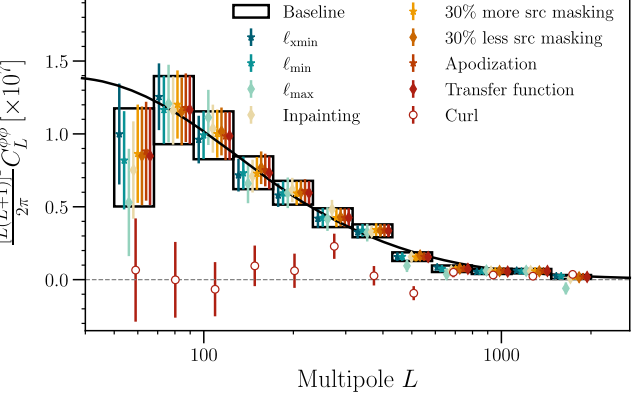


FIG. 6. Results of the power spectrum consistency tests and curl null test for the minimum-variance lensing band powers formed by combining temperature data at 95 GHz and 150 GHz. The band powers and errors for the baseline analysis are between the alternate analysis choice and the baseline by displayed as boxes. The band powers obtained from the different analysis choices are plotted with different colors and are in agreement with the baseline results. Note that we do not subtract the fiducial foreground bias template from these band powers.

TABLE IV. Consistency tests<sup>2</sup> xand PTEs.

Testname	X <sub>MV</sub>	PTE	ΔΑ <sub>ΜV</sub> σδΔΑ <sub>ΜV</sub> Þ	PTE
I <sub>xmin</sub>	15.1	0.24	-0.017 0.014	0.32
I min	13.8	0.30	0.003 0.003	0.33
I <sub>max</sub>	19.1	0.09	-0.032 0.043	0.42
Less inpainting	27.7	0.01	0.001 0.012	0.90
More masking	13.7	0.30	0.004 0.006	0.50
Less masking	24.6	0.03	0.011 0.006	0.05
Apodization mask	13.2	0.37	0.001 0.005	0.28
Transfer function	14.4	0.29	-0.002 0.002	0.54
Curl	16.0	0.18	-0.038 0.044	0.40

Summary of the  $\chi^2$  for the difference band powers and the difference amplitudes as well as their corresponding PTEs for the systematics tests.

correction, we stipulate that the PTE values should exceed the threshold of 5%=N, with N ¼ 9 here being the number of tests carried out [67] Here the different tests are being regarded as independent or weakly dependents.can be seen in Table IV, all our PTE values are above  $0.05=9 \approx 0.006$ . We conclude that we find no signs of significant systematic biases in these tests.

In Fig. 7, we present a visual overview of the consistensetting, scaled by the uncertainties of the respective down tests, illustrating the band power difference relative to the powers. The error bars represent the standard deviations of the baseline resultor each test. The error bars represent the variations derived from the distributions of simulationdifference bandpowers. In each L bin, the data points and estimators. error bars are normalized by the 1 $\sigma$  lensing spectrum uncertainties in that specific bin. We find that the difference band powers statistically meet expectations with no major systematic shifts for any test. Below, we discuss the results We mask and inpaint extragalactic pointsources and of each consistency test in more detail.

Varying I<sub>xmin</sub>, I<sub>min</sub>, and I<sub>max</sub>: The goals of these tests against contaminations. Our baseline analysis excludes modes I; I  $_x$  < 300 at 95 GHz (and I; I  $_x$  < 500 at 150 GHz) and modes at > 3000 for both 95 GHz and 150 GHz. We increase I<sub>min</sub> and I<sub>xmin</sub> by 200 and reduce I <sub>max</sub> by 500 compared to the baseline choices. When varying I<sub>max</sub>, we find the lensing spectrum using h<sub>ax</sub> 1/4 2500 to be consistent with hax 1/4 3000 at a PTE of 0.09. Also, the cumulative S=N ratio for lensing measurements inpainting for fainter sourcesby inpainting 50% fewer does not go up significantly beyond I ¼ 3000so we set I max cut also helps reduce the foreground biashich we estimate in Sec. IV E. For the lower I andend, we found  $I_{min} \frac{1}{4} I_{xmin} \frac{1}{4} 300 \text{ for } 95 \text{ GHz} \text{ (and } 500 \text{ for } 150 \text{ GHz)}$ to be an optimal threshold that reduces low-frequency instrumentaland atmospheric noise leakage into other I ranges ([31]) while not removing too many mode From Table IV, the lensing spectra afterchanging the I<sub>min</sub> or 0.24, respectively.

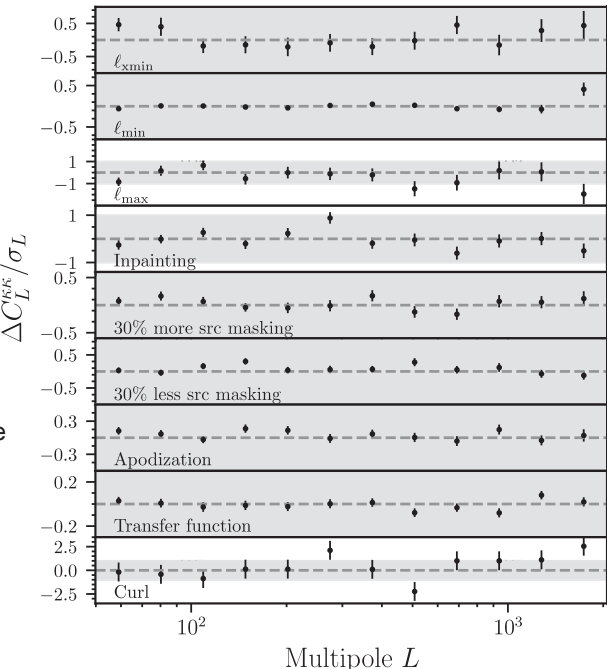


FIG. 7. Comparison of difference bandpowers (A)Obetween the baseline analysis and those where we vary a given analysis shifts for 340 simulations with the same analysis choice change. The shaded gray regions represent the  $1\sigma$  bands of the  $\phi^{TT}$ 

# 1. Source masking and inpainting

galaxy cluster imprints in the CMB map to reduce the bias they contribute (Sec. II E). We perform severaltests to include checking the reconstruction with different amounts determine whether the masking or inpainting thresholds of CMB modes and confirming the robustness of the results sufficient. Note that this is separate from the TOD-level masking discussed in Sedl. B, which is validated with a separate end-to-end analysisTo explore the impact of masking, we tune the flux threshold of point source masking such that 30% more or 30% fewer sources are masked compared to the baseline. The modified cuts correspond to flux thresholds of 47 mJy and 80 mJy compared to the baseline of 50 mJy at 150 GHz. We also test the impact of sources than the baselineThe modified cuts correspond this as the high-I limit for our baseline analysis. Setting anto source flux thresholds of 6.0 mJy, 6.0 mJy, and 12.0 mJy at 95 GHz, 150 GHz, and 220 GHz and cluster detection significance threshold of 9, compared to the baseline choices described in Sec. II E. The PTEs for bandpower difference relative to the baseline are 0.30 for 30% more masking, 0.03 for 30% less masking, and 0.01 for 50% less inpainting. We note that the data points in Fig. 7 do not move much relative to the baseline results despite the relatively small PTEs for less I xmin are consistent with the baseline with PTEs of 0.30 amdasking and less inpainting, which indicate that the change in the bandpower is larger than expected from the sims given

the same analysis chang&till, the bandpower PTEs are spectrum for the amplitude calculation. Second, no MC consistent with expected changes from the simulations aftersponse correction from simulations is applied to the we account for the Bonferroni correction. Furthermore, the econstructions since the expected signal is zero. lensing amplitude PTEs for less masking and less inpainting lowing the method for the lensing spectrum analysis, are 5% and 90%, respectively. We conclude that our results correct for other biases to the curl spectrum, including are robust to variations of masking and inpainting choicesthe nonzero N bias from the lensing trispectrum [25]. We

# 2. Mask apodization

Gradients in the masking edges can mimic lensing and be captured by the lensing estimator. The mean field subtraction discussed in SetVA should correct for this bias. To check whether the bias from mask apodization is negligible, we change the cosine taper radius for the boundary mask from the baseline of 300 to 600 and the source mask from 10<sup>0</sup> to 20<sup>0</sup>. We repeat the complete analysis process with these changes and find the data difference to agree with the simulation difference distribution with a PTE of 0.37.

# 3. Transfer function variation

The goal of this test is to confirm our analysis is of the transfer function by estimating the transfer functionshe beam profile across the entire multipole range. The using another set of Gaussian simulations following a powerulting systematic shiftn the amplitude of the lensing law spectrum with a spectral index of −1 instead of the CMBwer spectrum is  $\Delta A_{beam} 1 0.013$ , which is 22% of the power spectrum following the method described in Sec. Ilstatistical uncertainty on Av. The new transfer function has different mode coupling and shifts slightly compared to the baseline transfer function due to a change in the map spectra used to estimate it. We expect the impact to be small because of the response normalization. We use a temperature calibration factor to calibrate the discussed in Sec.IVA. Using a slightly varied transfer function should only result in a nonoptimal weighting and small degradation of S=N ratio. The power spectra using the the Gallousing simulations with the same baseline transfer function and the new one are consistent noise levels. The uncertainties forthe four subfields are with a PTE of 0.29.

#### 4. Curl test

The lensing deflection field d can be decomposed into gradient and curl components: dốn μ ¼ ∇φο μ þ  $\eth$ \*∇ÞΩ $\eth$ Þ, where  $\Phi$  is the lensing potential,  $\Omega$  is the divergence-free or curl component, and ★ is a 90° rotationdifference by conducting the baseline analysis with the operator [68]. We expect the curl component to be zero atemperature calibration of the data maps shifted by 1σ, our reconstruction noise levelswhere higher-orderand post-Born effects are negligible [69]. However, foregrounds or other systematic effects may introduce a nonzero curl signal to the dataA curl estimation on the data can test for these signals. The curl spectrum  $C^{\Omega\Omega}$  is extracted using an estimator analogous to the lensing distinctions. First, the theoretical input is set to a flat spectrum  $\mathbb{Q}^{\Omega}$  1/4 10<sup>-7</sup>, which is used to uniformly weight the modes when binning, as well as to establish a referencely SPT-SZ measurements.

plot the curl spectrum for the MV combination in Fig. 6. which is consistent with null ata PTE of 0.18.

## D. Systematic uncertainties

In this subsection, we assess the impact of uncertainties in the beam measurement and temperature calibrations on the lensing amplitude measurement.

# 1. Beam uncertainty

To assess the impact beam-related uncertainties we introduce perturbations to the baseline beam profile using the uncertainties ( $\Delta B$ ) obtained from [31]. These perturbations are applied by multiplying 1 þ Δ Bo the data map while keeping the simulations unchangedSubsequently, insensitive to variations in transfer functions estimated using divide both the data and simulations using the baseline input maps with different power spectra. We test the impasseam, which tests for a systematic 1σ underestimation of

# 2. Temperature calibration

raw temperature maps via T  $\frac{1}{4}$  T  $\frac{1}{4}$  X T Cal. As outlined in Sec. II D, we calculate the uncertainty of the calibration similar. By taking their average, the uncertainties associated with  $T_{\text{cal}},\,\delta T_{\text{cal}},$  are 0.3% and 0.2% for 95 GHz and 150 GHz, respectively. While keeping the simulated maps unchanged, we adjust the data maps by scaling them with (1 þ δT<sub>cal</sub>) for the temperature mapand subsequently reevaluate the data lensing amplitudes. We then quantify the resulting in a  $\Delta A_{cal}$  ¼ 0.010 for the MV reconstruction, or about  $0.16\sigma$  of the statistical uncertainties.

We report the quadrature sum of the beam and temperature calibration uncertainties as the total systematic uncertainty in Table III. The total systematic uncertainty is 0.016, which is smaller than the statistical uncertainty of 0.060. This is estimator introduced in Sec. IVA but designed to respondsmaller than SPTpol's systematic uncertainty of 0.040 due to to the curl component [68]. In addition, there are two key the absence of polarization calibration uncertainty, SPTpol's leading source of systematic uncertainity, our case. Our systematic uncertainty is similar to that of the temperature-

#### VI. COSMOLOGICAL PARAMETERS

In this section, we present constraints from the 2018 SPT-3G lensing power spectrum on ΛCDM cosmological parameters as well as on a number of one- and twovariance lensing band powers from temperature data introduced in Sec. IV D to carry out the cosmological inference.

# A. Cosmological inference framework

family of massive neutrinos having a total mass of m<sub>v</sub> ¼ 60 meV<sup>5</sup> The model is based on purely adiabatic correction factor [77]. scalar fluctuations and includes six parameters: the physical The lensing potential power spectrum estimate depends density of baryons (\$\Pma^2\$), the physical density of cold dark on cosmology through the response functionand on the matter  $(\Omega h^2)$ , the (approximated) angular size of the sound  $h_1^1$  bias as horizon at  $recombination(\theta_{MC})$ , the optical depth at reionization (τ), the amplitude of curvature perturbations at k  $\frac{1}{4}$  0.05 Mpc<sup>-1</sup> (A<sub>s</sub>), and spectral index (n<sub>s</sub>) of the power law power spectrum of primordial scalarfluctuations. We also quote constraints derived from these main where  $\Theta_{fid}$  denotes the fiducial cosmology assumed to six parameters, such as the square root of the variance of perform the lensing reconstruction. Here, we follow the density field smoothed by a sphericator hat kernel with a radius of 8 Mpc=h, as calculated in linear perturbation theory [70], and the Hubble constantH<sub>0</sub>. We then examine a series of ACDM extensions including the sum the neutrino masses  $m_v$  and the spatial curvature  $\Omega_k$ . The lensed CMB and CMB lensing potential power spectra to the primary CMB power spectra (in our case only CMB) are calculated with the AMB Boltzmann code. We sample the posterior space and infer cosmological parameter constraintsusing the Metropolis-Hastings sampler with adaptive covariance learning provided in the Markov Chafiducial cosmology and stored in the matrices Mn and Monte Carlo (MCMC) Cobaya package.

# 1. Lensing likelihood

number of relativistic species with N 1/4 2.044.

https://github.com/CobayaSampler/cobaya.

where C<sub>h</sub><sup>φφ;th</sup>ðΘÞ is the binned theory lensing spectrum evaluated at the position  $\Theta$  in the parameter space, as given by the Boltzmann solverWhen combining CMB lensing measurements with primary CMB datage neglect correparameter extensions. As a reminder, we use the minimulations between the 2- and 4-point functions as these have been shown to not affect the cosmological inference at current noise levels [73–76]. Therefore, when jointly analyzing CMB lensing and primary CMB, we simply multiply the respective likelihoods. As discussed in Sec. IV D, the covariance matrix for the minimum-variance lensing binned spectrum is calculated using Monte Carlo Our baseline cosmology is a ACDM model with a single simulations from the conditioned covariance matrices. We rescale the inverse covariance matrix by a ≈4% Hartlap

Bianchini et al. [2] Sherwin et al. [15], Planck Collaboration etal. [20], Simard etal. [78] and take this cosmological dependence into account by linearly perthrbing  $R_L$  and  $N_L^1$  around  $\Theta_{fid},$  which amounts to calculating derivatives of the response function with respect and of the N<sub>1</sub><sup>1</sup> bias with respect to the lensing potential spectrum  $\stackrel{\Phi}{\mathcal{C}}$ . These corrections are computed once for the  $M_{ph^0}^{\phi\phi}$ , respectively. Including the contribution from residual foregrounds, the full prediction for the lensing potential power spectrum takes the following form:

where summation over bis implied. In Eq. (23),  $C_{\phi}^{\phi,fg}$  is the foreground contamination template introduced in Sec. IV E and A is the corresponding amplitude parameter <sup>5</sup>The massless neutrino species contribute to the total effective which we impose a uniform prior A<sub>fg</sub> ~ Uŏ0; 3ÞThe prior range is motivated by the approximately factorof three difference between the foreground biases estimated from AGORA and from van Engelen et al[58].8

https://camb.info (v1.4.1). We use the Mead model [71] to calculate the impact nonlinearities on the small-scale matter power spectrum Pδδ kp. The accuracy settingsof CAMB are set to lens\_potential\_accuracy=4; lens\_margin =1250; AccuracyBoost =1.0; ISampleBoost =1.0; and IAccuracyBoost = 1.0, which have been shown to be accurateenough for current sensitivities while enabling fast MCMC runs (see Qu etal. [3], Madhavacheriet al. [72], and references therein).

<sup>&</sup>lt;sup>8</sup>The masking thresholds and noise levels are different in van Engelen et al. [58] so we do not expect it to be representative of the foreground bias in our measurementHowever, it is a reference point of how different simulations with different assumptions of astrophysics can produce factor of a few difference in the level of foregrounds biases.

# 2. Cosmological datasets

from a comprehensive analysis of three main classes of cosmological observables. Our study incorporates the following key observables and survey data:

- (i) CMB lensing: We use the 2018 SPT-3G lensing along with the lensing bandpowers obtained from the analysis of the Planck CMB PR4 (NPIPE) maps [22]. The SPT-3G and Planck datasets have diffe sensitivities to different components of the primar CMB due to their limited overlap in the observational footprints (3.6% compared to 67% of the sky and different noise properties and angular resoluti These two datasets are therefore relatively independent dent. Additionally, we compare the new constrain from SPT-3G to the previous results from the SPTpol experiment presented in Bianchini et al. [2] and SPT-SZ in Simard et al. [78]. The constrai in Bianchini et al. [2] and Simard et al. [78] are based on the lensing measurements W19 and O17, respectively.
- MGS [Sloan Digital Sky Survey Main Galaxy Sample: [80]], 6dFGS [Six-degree Field Galaxy Survey; [81]], and eBOSS DR16 Luminous Red Galaxy [LRG, [82]] surveys. Incorporating inforus to refine the parameter constraints in the  $-\Omega_0$ plane and gain insights into the amplitude of the large-scale structure.
- Primary CMB: As our baseline early universe observable, we employ the power spectrum meazation anisotropies from the Planck 2018 data release [83]. Specifically, we use the low- and high-I temperature and polarization likelihoods from PR3 maps. In addition, we make use of the 2018 SPT-3G TT=TE=EE intermediate and smallscale measurements from Balkenhol et 233.

# B. Constraints from CMB lensing alone

We start by considering constraints on ΛCDM parameters from CMB lensing measurements alone, with a special focus on the amplitude of matter fluctuations.

The parameters that ve vary in this analysis and their

TABLE V. Cosmological parameters varied in this work and In this work, we present parameter constraints obtained their respective priors. Parameters that are fixed are reported by a single number. Uða; bÞ denotes a uniform distribution between ½a; b, while N ðµ; ♂Þ indicates a Gaussian distribution with mean u and variance & In addition to these we include and marginalize over the amplitude of the foreground bias template using a uniform prior A<sub>fg</sub> ~ Uŏ0; 3ÞNote that when adding power spectrum measurement presented in this workimary CMB information from SPT-3G,we adopt a Planck based Gaussian prior on τ ~ N δ0.0540; 0.007.4

ereRarameter	Lensing only (þBAO)	Lensing b CMB
$\Omega_{ m b} h^2$	N ŏ0.02233; 0.0003b	Uð0.005; 0.1Þ
$\Omega_c^2$	Uð0.005; 0.99Þ	Uð0.001; 0.99Þ
$(y)H_0$ [km=s=Mpc]	Uð40; 100Þ	Uð40; 100Þ
tiom.	0.055	Uð0.01; 0.8Þ
ena <sub>s</sub>	N ð0.96; 0.0 <b>2</b> Þ	Uð0.8; 1.2Þ
nts ந∂10⁰A <sub>s</sub> Þ	Uð1.61; 3.91Þ	Uð1.61; 3.91Þ
m <sub>v</sub> [eV]	0.06	0.06 or Uð0; 5Þ
$\Omega_{K}$	0	0 or Uð−0.3; 0.3Þ
int <del>\$</del> ∟	1	1 or Uð0; 10Þ
$A_L^{\phi\phi}$	1	1 or Uð0; 10Þ

(ii) BAO: We utilize likelihoods obtained from spectro- that we fix T 1/4 0.055 [34], since CMB lensing is not scopic galaxy surveys, including the BOSS (Baryondirectly sensitive to the optical depth, and that we impose a Oscillation Spectroscopic Survey) DR12 [79], SDS Saussian prior on the baryon density Ω ½ ¼ 0.02233 0.00036 based on recent element abundances and nucleosynthesis (BBN) modelling [84,85] as wells an informative albeit wide prior on Planck CMB anisotropies power spectra [34]. When analyzing SPT-3G CMB lensing mation about the BAO scale into our analysis allowsneasurements without primary CMB power spectra, we fix the linear corrections to the response function to the fiducial cosmology and only vary the ones related to the Naias.

Within the base ACDM model, constraints from CMB lensing measurementalone follow a narrow elongated tube in the 3D subspace spanned by  $\Phi I_0$ - $\Omega_m$ . This is surements of primary CMB temperature and polari-then projected as an elongated narrow region on the  $\Omega$ plane, as shown in Fig. 8. The parameter combination optimally determined by CMB lensing measurements is  $\sigma_8\Omega_m^{0.25}$ , which is constrained from SPT-3G data at the ≈4.4% level:

$$\sigma_8 \Omega_m^{0.25} \frac{1}{4} 0.595 \ 0.026 \ \text{ dSPT-3GP}$$
:  $\text{d}24\text{P}$ 

As a simple and quick way to estimate the agreement between measurements from two (independent datasets. we calculate the differences in centralparametervalues normalized to the sum in quadrature of the uncertainties:  $\delta\mu_1 - \mu_2 \triangleright = \frac{\sigma_1^2}{\sigma_1^2} \rho \sigma_2^2$ , where  $\mu$  and  $\sigma$  are the central values corresponding priors are listed in Table V. Note in particuland variances of the two measurements, respectively. With this definition,  ${\tt g}\Omega_{\tt m}^{0.25}$  inferred from SPT-3G is only 0.13 ${\tt \sigma}$ 

<sup>&</sup>lt;sup>9</sup>While CMB temperature and polarization power spectra mostly probe the early Universe at  $z \approx 1100$ , we stress that secondary interactions like lensing eionization, and the inteevolution.

<sup>&</sup>lt;sup>10</sup>See,e.g., Planck Collaboration etal. [20], Madhavacheril et al. [72], Pan et al. [86] for pedagogical discussions on the grated Sachs-Wolfe effect confer sensitivity to the low-z universesmological parameter dependence of the CMB lensing power spectrum.

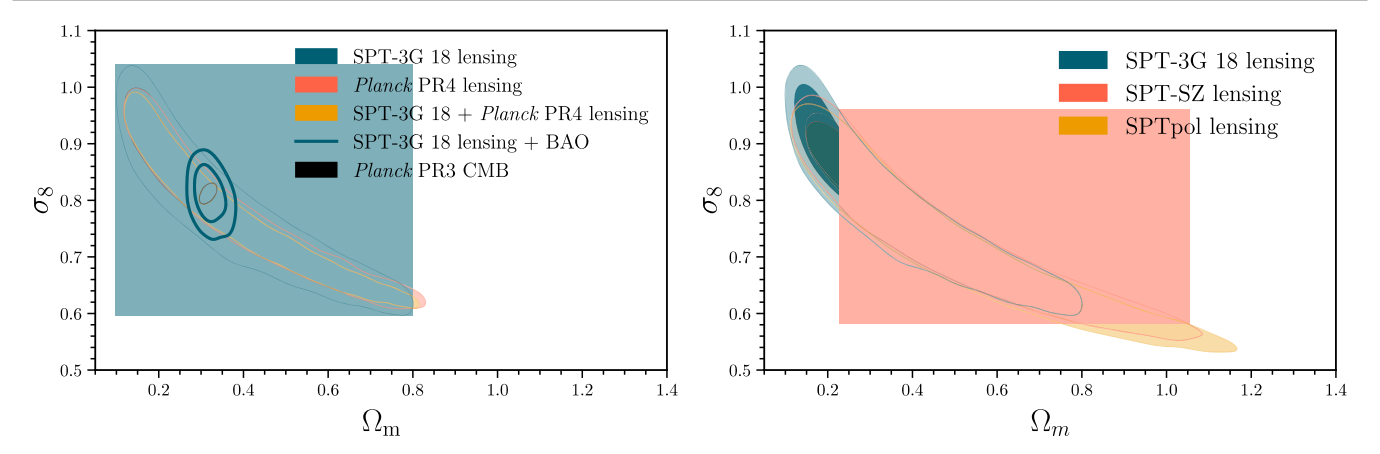


FIG. 8. Left: Constraints in the Ωσ<sub>8</sub> plane from our SPT-3G CMB lensing measurements (filled blue contours). For comparison, we also include results from Planck PR4 lensing (red contours) as well as its combination with SPT-3G lensing data (yellow contours). The empty blue contours show the constraints combining outPT-3G lensing likelihood with BAO data. The black filled contours representing the independent constraints derived from the Planck primary CMB power spectra are also found to be consistent with the CMB lensing measurements between redshifts Right: Comparison of  $\Omega$ - $\sigma_8$  constraints across difference to surveys.

away from the Planck PR4 lensing value of  $\sigma_8 \Omega_{\rm m}^{0.25} \frac{1}{4}$ 0.599 0.016 and also in agreement at the 0.5 $\sigma$  level with constrains particularly well, the combination  $\sigma_8\Omega_m^{0.25}$  ½ the value of  $\alpha\Omega_{\rm m}^{0.25}$  ¼ 0.609 0.008 based on the Planck CMB PR3 anisotropies.

In the right panel of Fig. 8, we compare the SPT-3G results with those from the SPT-SZ analysis in [27] and the tails of the foreground treatment For example, when SPTpol analysis in [28]. It is important to note that apart from using three different cameras these SPT measurements differ in other aspectsas well. Firstly, the sky coverage of these measurements are differer & econdly. while this measurement is similar to the temperature-only in the central value.

SPT-SZ analysis in that it relies solely on temperature data. We then proceed to combining the SPT-3G and the [28] measurementsed both temperature and polarization data, with the latter carrying more statistical weight (Sec. VI A 2) and the consistency of the SPT-3G and in the final result. Lastly, the SPT-3G and SPT-SZ lensing Planck measurements their combination then involves a power spectra extend to lower multipoles (L 1/4 50) than the traightforward multiplication of the lensing likelihoods SPTpolmeasuremen(L 1/4 100). Hence, the SPT-3G and SPT-SZ measurements are more similar in that both area, whereas SPT-3G and SPTpol provide relatively independentssessments of cosmology.

As can be seen from the right panel of Fig. 8, the main reported in Table VI. difference between the SPT-3G dataset and its predecessors is that the bulk of the posterior mass moves to a region of the parameter space with lower, and higher g, excluding the high-Q tail present in the SPT-SZ/SPTpol datasets. Next, we turn our attention to the cosmological implica-In particular, SPT-3G prefers a higherprimordial scalar spectrum amplitude (Α), a parameter closely related to σ with  $\log \delta 10^{10} A_s > 1/4 \ 3.22_{0.23}^{0.27}$  than what is preferred by either SPT-SZ, at 2.76\_{0.28}^{0.28}, or SPTpol, at 2.65 0.35. While bandpower fluctuations can lead to higher or lower

preferred  $\Omega$  and  $\alpha$  values, neither of which CMB lensing 0.595 0.026 from SPT-3G is in good agreement with the values from SPTpol and from SPT-SZ.

We also note that our constraints are robust against fixing the amplitude of the foreground contamination template  $A_{fg}$  to unity, the inferred constraint on the amplitude of structure becomes  $\Omega_{\rm m}^{0.25}$  ¼ 0.589 0.024, only a 8% reduction in uncertainty and less than 0.25σ shift

Planck lensing measurementsGiven the independence associated with each datase the constraint on  $\Omega_m^{0.25}$  1/4 0.596 0.014 is improved by about 13% with respect to use temperature data and cover a largely overlapping skyPlanck lensing-only statistical uncertainties. A summary of the marginalized  $\mathfrak{g}\Omega_{\mathsf{m}}^{0.25}$  constraints across different datasets is provided in Fig. 9 and the numerical values are

# C. Constraints from CMB lensing and BAO

tions that arise from the inclusion of BAO data with CMB lensing measurements. In addition to providing constraints on  $\alpha$  and  $\Omega$ <sub>n</sub>, the CMB lensing power spectrum is sensitive to the expansion rate of the to its influence on the parameter combination  $\Omega_m^{0.25} \delta \Omega_m h^2 \dot{D}^{0.37}$  [20,72,87]. Within ΛCDM, the CMB lensing power spectrum can be written as an integral over the matter power spectrum

 $<sup>\</sup>overline{}^{11}$ We have rerun the chains for the SPT-SZ and SPTpol surverset; zPAs a result,  $C_L^{\varphi\varphi}$  is sensitive to the broadband adopting the same priors and BAO dataset used in this analysishape of Rook; zb, which is mostly controlled by the scale of

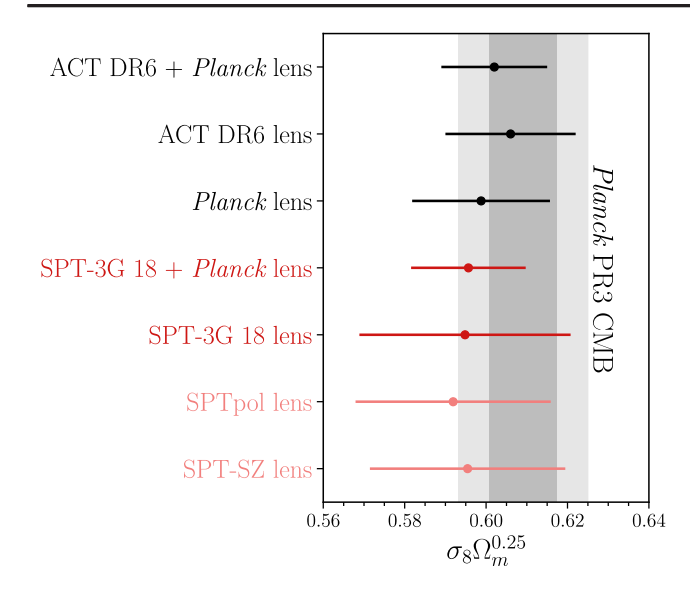


FIG. 9. Marginalized  $\alpha \Omega_m^{0.25}$  posterior across different SPT, errors from Planck PR3 CMB temperature and polarization anisotropies.

matter-radiation equality  $k_{eq} \equiv a_{eq} H_{eq} \propto \Omega_m h^2$  and the primordial amplitude A. The shape and amplitude of the matter-radiation equality scale  $k_{eq} = k_{eq} \times \Omega_m^{0.6}h$ , and  $k_{eq}$ is reconstructed and by the range of scales the lensing measurement probes. Therefore, by effectively providing potential inaccuracies on the MF estimate/hen discardhandle on  $\Omega_{\rm fl}$ , measurements of the projected BAO scale ing the first two bins of the measured SPT-3G lensing from low-z galaxy surveys can break theΩη-H<sub>0</sub> degeneracy and sharpen constraints on the individual parametets< 92), the parameter constraints become:

In Table VI, we report constraints from CMB lensing and BAO on  $\sigma_{8}$ ,  $\Omega_{m}$ , and H<sub>0</sub>. For our baseline SPT-3G measurementwe find the following constraints:

$$H_0$$
 ½ 68. $\&_{1.6}^{1.3}$  km  $\bar{s}^1$  Mpc<sup>-1</sup>  $=$   $\sigma_8$  ½ 0.810 0.033 SPT-3G lensing  $\bar{p}$  BAO:  $\Omega_m$  ½ 0.32 $\&_{0.026}^{0.021}$ 

The  $\sigma_8$  and  $\Omega_m$  parameters are constrained at the 4% and 7% levels, respectively, and are both consistent (central values well within  $1\sigma$ ) with the values inferred by the Planck primary CMB and lensing measurements. The combination of SPT-3G CMB lensing, BAO, and BBN prior yields a ≈2% constraint on the expansion rate ith a central value of 68.8 km s

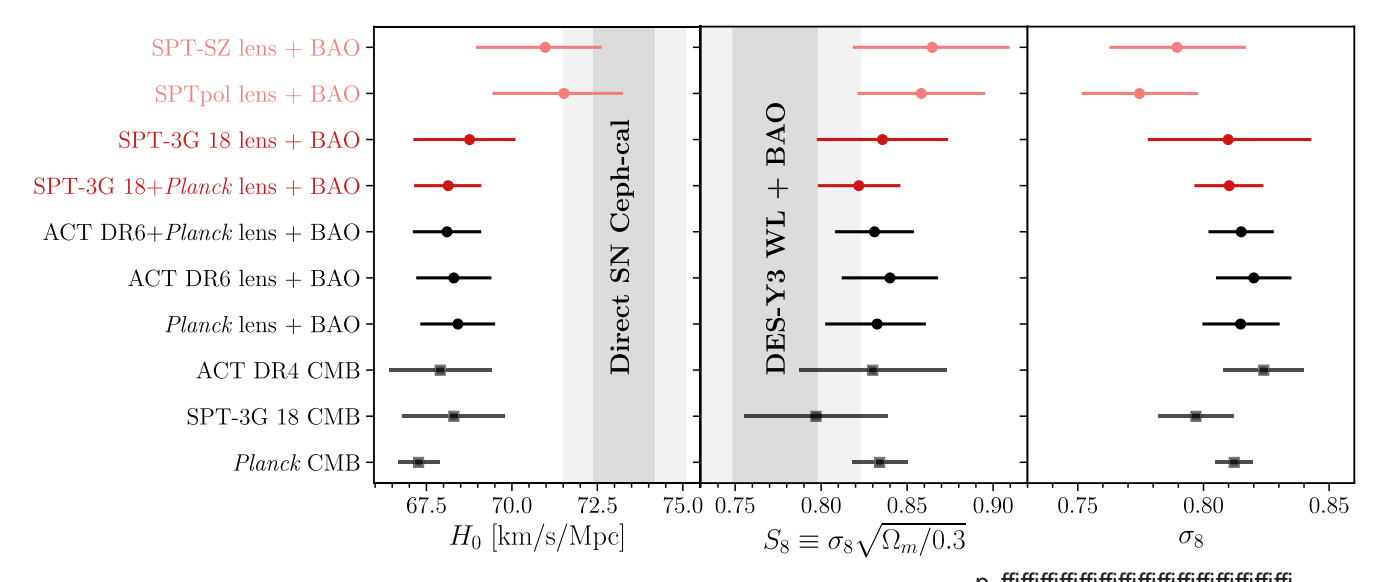
1 Mpc

1. This value is con-Planck, and ACT CMB lensing measurements. The shaded darkistent with other CMB lensing- and primary CMB-based and light gray regions denote respectively the 1 and 2σ statistical constraints of the Hubble constant within the ΛCDM model (see Fig. 10), as well as the TRGB-calibrated local distance ladder measurement of Freedman et al. [88]. When compared to recentdirect H<sub>0</sub> constraints from Cepheidcalibrated SH0ES supernovae (SN) measurements [37], we CMB lensing potential power spectrum are thus sensitive to We explore the sensitivity of our results to the low-L bins adaptor to the sensitivity of our results to the low-L bins. a degenerate combination of the multipole corresponding to and foreground marginalization. We compare our baseline result [Eq. (25)] to ones without the lowest L bins because [or  $\sigma_8$ , see, e.g., [2,20,72,86]]. The precise extent of the Athe magnitude of the MF bias surpasses that of the signal I eg parameter degeneracy is dictated by how accurately Gor scales below L ≤ 100 (see Fig. 2), which might lead one to question the robustnessof the baseline result given power spectrum (i.e. throwing away information below

$$H_0$$
 ½ 68.9 1.6 km s<sup>-1</sup> Mpc<sup>-1</sup>  $\stackrel{9}{=}$   $\sigma_8$  ½ 0.809 0.033 , SPT-3G lensingðl<sub>min</sub> ½ 92Þ þ BAO: Ď26Þ  $\Omega_m$  ½ 0.32 $\rlap{\sl}^{0.027}_{0.030}$ 

TABLE VI. Constraints on a subset of ΛCDM parameters using the Planck and SPT-3G CMB lensing datasets alone, jointly analyzed, or combined with BAO information. All intervals quoted in this table are 68% intervals, H is in units of km s<sup>-1</sup> Mpc<sup>-1</sup>.

	Lensing		Lensing + BAO			
	$\sigma_8\Omega_{\rm m}^{0.25}$	$\sigma_8$	H <sub>0</sub>	$\Omega_{m}$	S <sub>8</sub>	
SPT-3G 18	0.595 0.026	0.810 0.033	68.8 <sup>1.3</sup>	0.3200.021	0.836 0.039	
Planck	0.599 0.016	0.815 0.016	68.4 1.1	0.313 0.015	0.833 0.029	
SPT-3G 18 + Planck	0.596 0.014	0.810 0.014	68.1 1.0	0.309 0.014	0.822 0.024	
SPT-SZ	0.597 0.024	0.789 0.027	71. $\mathfrak{C}^{1.7}_{2.0}$	$\begin{array}{c} 0.36  \stackrel{1}{\cancel{}}_{0.033}^{0.028} \\ 0.36  \stackrel{1}{\cancel{}}_{0.035}^{0.029} \end{array}$	0.865 0.041	
SPTpol	0.592 0.024	0.775 0.023	71. $\mathfrak{L}^{1.7}_{2.1}$		0.858 0.037	



different cosmological probes and surveys The direct  $H_0$  measurements taken from Murakamiet al. [37], while the LSS-based constrainton S<sub>R</sub> is taken from the reanalysis of the DES-Y3 (+ BAO) data of [40] presented in Madhavacheal. (§72].

While the uncertainties on some of the parameters slightly deteriorate the inferred central values are largely unchanged. The parameter that is affected most is  $\Omega_{\rm m}$ , whose  $1\sigma$  uncertainty is degraded from  $0.024 \rightarrow 0.028$ , followed by  $\sigma \delta H_b \triangleright \frac{1}{4} 1.5 \rightarrow 1.6$ . We also find foreground marginalization does notdramatically affect the cosmological inference. We test this by setting A fa 1/4 1 and

repeating the MCMC analysis. The parameterthat is affected mostby the change is a for which we find an updated 1 $\sigma$  constraint of  $\sigma$ 4 0.80 $\sigma$ 0.029. As can be seen, the shift in the central value is 0.15 $\sigma$  and the  $\sigma$ 4 and  $\sigma$ 5 are  $\sigma$ 6.000 updated 1 $\sigma$ 6.000 updated 1 $\sigma$ 7. marginalization degrades the sensitivity by about 17%.

The constraints in Eq. (25) are sharpened when lensing information from Planck PR4 lensing is included:

$$H_0$$
 ¼ 68.1 1.0 km s<sup>-1</sup> Mpc<sup>-1</sup>  $\stackrel{9}{=}$   $\sigma_8$  ¼ 0.810 0.014 ; SPT-3G lensing  $\flat$  planck lensing  $\flat$  BAO:  $\check{o}$ 27 $\flat$   $\Omega_m$  ¼ 0.309 0.014

There are severalntriguing differences between these results and those from the previous SPTpalnd SPT-SZ lensing b BAO analyses. Firstly, as shown in Tab. VI, the SPT-SZ and SPTpol. Intersected by the BAO contours, precision of constraints on Ω and H<sub>0</sub> obtained from SPT-3G improves by approximately 30% when compared to the avor a high value of H<sub>0</sub> ¼ 72.7-2,9, gives the resulting corresponding values from SPTpoand SPT-SZ.The σ<sub>8</sub> due to foreground marginalizationSecondly,the central values for the Hand  $\Omega_n$  obtained through SPT-3G lensing thorough analysis of the consistency across the various shift towards lower values than those from SPTpoland improvement in the precision of  $\Omega_m$  and  $H_0$  is in part explained by the decrease in the  $\sigma_8$ -H<sub>0</sub>- $\Omega_m$  posterior of the lower noise in SPT-3G compared to SPT-SZ and the foreground template to QAV4 0 (i.e. neglecting residual the larger area/lower hin compared to SPTpol). The shift foreground contamination in the lensing reconstruction) to a lower central H value can be understood as follows. suppresses the lensing powerly about 5% and slightly

lower  $\Omega_m$ -H<sub>0</sub> (and higher A and  $\Omega_m$ ) relative to those from which are positively correlated in the  $\Omega_{\!m}\text{-H}_0$  plane and  $\Omega_{\rm m}$ -H<sub>0</sub>- $\sigma_{\rm 8}$  combinations, with lower H[e.g. [89]]. In other uncertainties are degraded by 20–30% compared to the words, the high ₩ preference from BAO-alone constraints other two SPT results, which is shown above to be largely is more effectively pulled down by SPT-3G's combination of a smaller and shifted posterior subspace. While a SPT lensing measurements requires common simulations SPT-SZ while g increases slightly, mirroring the shifts of to properly account for the correlations and is beyond the  $\Omega_{m}$  and Q from lensing-alone constraints in Sec. VI B. Thescope of this work, we note that reasonable shifts in the tilt and amplitude as well as the magnitude of the uncertainties, within the SPT-3G measurementrive ≤1σ shifts in volume in SPT-3G compared to SPT-SZ /SPTpol (becauste parameter space. As an example, fixing the amplitude of

perturbs the spectrum tilacross the whole  $L \in \frac{1}{2}50$ ; 2000 range. As a consequence, the corresponding central values In the following sections, we study the consistency of the relevant parameters from SPT-3G move towards the SPT-SZ/SPTpolconstraints (but not completely) and become  $\Omega_n$  ¼ 0.33 $\mathfrak{C}_{0.028}^{0.024}$ ,  $\sigma_8$  ¼ 0.783 0.029, and  $H_0 \frac{1}{4} 69.3_{1.6}^{1.5}$ 

In order to compare our constraints with the findings from optical weak lensing surveys, we also provide the infinition of Table V and include both the response inference on  $\S$ , which is defined as  $\sigma_8$   $\Omega_m$ =0.3 This parametercombination is known to be most accurately estimated from galaxy shear measurements and has recently been the subject of intense scrutiny due to  $2 - 3\sigma$  tensions between the primary CMB and galaxy lensing constraints e.g., [90]. From SPT-3G lensing data ineionization of T 1/4 0.0540 0.0074 (which is primarily combination with BAO scale information, we find a 4.7% determination of the parameter at the level

or S<sub>8</sub> ¼ 0.822 0.024 when jointly analyzed with Planck lensing data. Note that these statisticaluncertainties are smaller than the typical errors from current galaxy lensingthrough, e.g., the smearing of the acoustic peaks in the surveys such as the Dark Energy Survey<sup>12</sup> [DES-Y3, [40,91,92]], the Hyper Suprime-Cam Subaru Strategic Program<sup>3</sup> [HSC-Y3, [93,94]], and the Kilo Degree Survey  $^{14}$  [KiDS-1000, [38]]. The S<sub>8</sub> value favored by SPT-3G lensing b BAO is approximately 1.7d, 6σ, and 1.8σ higher than that from DES, HSC-Y3, and KiDS, respectively. We note that the precision of gurosstraint from CMB lensing and BAO is slightly better than that achieved using primary CMB information from SPT-3G,  $S_8 \frac{1}{4} 0.797 \quad 0.042 \quad [33]$ , with the central value from CMB lensing b BAO being about 0.7σ higher.

the Hubble constant 닭 S<sub>8</sub>, and ஒ across different probes and surveys is provided in Fig. 10. We choose two representative values in the literature to highlightdirect H<sub>0</sub> and LSS § measurements. Our results are in excellent uncertainties in the foreground cleaning. We first fix the agreementwith the ACT DR6 and Planck lensing constraints. For H, we show the result from Murakami et al. [37],  $H_0 \frac{1}{4}$  73.29 0.90, which currently maximizes the  $5.7\sigma$  level, while for the low-z amplitude of structure we so-called 3 × 2 pt) measurements from DES-Y3 [40]n combination with BAO data, as presented in Madhavachesibectrum amplitude normalized to the Planck 2018 et al. [72]. For completeness, we also point the reader to the TEEE+lowE+lensing fiducial recent results from HSC [93,94], KiDS [38], and the joint analysis of DES and KiDS data [95].

#### D. Constraints on ΛCDM extensions

between the amount of lensing favored by direct and indirect lensing measurements well as the impacton the sum of the neutrino massesm, and curvature density  $\Omega_{\rm K}$  constraints when including SPT-3 $^{\mbox{$\mbox{$}}\mbox{$\mbox{$}\mbox{$}\mbox{$}}\mbox{$\mbox{$}}$ the cosmological inference. We adopt the priors listed in the function and N linear corrections to the lensing likelihood, as discussed in Sec. VI A 1. Note that when replacing Planck primary CMB data with SPT-3G TT=TE=EE measurements from Balkenhoet al. [33], we impose a Planck-basedGaussian prior on the optical depth to constrained by a feature in the TE and EE spectra at I < 10).

# 1. Lensing amplitudes

Lensing imprints in CMB maps can either be reconstructed directly, for example by exploiting the induced higher-order correlations between Fourier modes to measure  $C_L^{\varphi\varphi}$  (the main focus of this paper), or indirectly primary CMB spectra.In this section, we compare direct and indirect CMB lensing measurements and ask ourselves two questions: 1) is the amplitude of the reconstructed lensing power spectrum consistent with the fiducial Planck ACDM cosmology; and 2) does the amount of lensing preferred by the primary CMB smoothing agree with the one suggested by direct lensing measurement?

We have already partially answered the former question in Sec. VB, where we have defined a lensing amplitude parameter  $A^{\circ}$  as a weighted rescaling of the meas  $\hat{\mathbf{Q}}_{i}^{\circ}$ with respect to a binned fiducial power spectrum. The A visual comparison of the marginalized constraints on lensing amplitudes in Sec. V B are directly corrected for the estimated foreground bias template, assuming its amplitude is exact and fixed to  $A_{fg}$  1/4 1. Here we revisit the lensing amplitude calculation using MCMC by marginalizing over lensing power spectrum to the assumed fiducial cosmology, C<sub>1</sub><sup>φφ</sup>ðΘ<sub>fid</sub>Þ, and then rescale it by an overall amplitude two free parameters,  $^{\phi}$ A and  $A_{\alpha}$  [defined in Eq. (23)], and pick the galaxy-galaxy lensing and galaxy clustering (the we include N bias correction in Eq. (23). When using the uniform prior on A ~ Uð0; 3Þ, we obtain a lensing power cosmology of

ð29Þ

which is consistent with unity within  $\approx 0.7\sigma$ . This value is about 4% higher than was found in Sec. V B

<sup>&</sup>lt;sup>12</sup>https://www.darkenergysurvey.org.

<sup>&</sup>lt;sup>13</sup>https://hsc-release.mtk.nao.ac.jp/. 14https://kids.strw.leidenuniv.nl.

and its associated uncertainty isdegraded by a factor of 1.5.<sup>15</sup>

The second question is perhaps more interesting since the amount of lensing determined from the smoothing of the acoustic peaks in the Planck temperature and polarization power spectra is largeat the  $2\sigma$  to  $3\sigma$  level, than what is predicted by ACDM and when compared to direct CMB lensing measurements e.g[34,96,97]. To complicate things furtherthe magnitude and significance of this anomaly vary between different Planck data releases and likelihood versions e.g., [98], and ground-based CMB surveys such as SPT and ACT do nobbserve a similar amount of 2-pt function smearing [33,99]. To check whether the SPT-3G lensing power spectrum is consistent

with the lensing information in the primary CMB 2-point to A₁<sup>φφ</sup>, we introduce a nonphysicaparameter A which reconstruction powerand the smoothing of the acoustic peaks.

In Fig. 11, we show the constraints on the lensing amplitude parameters from the jointanalysis of SPT-3G ropies. In the figure, the combination  $\mathbf{A}_{l}^{\phi\phi}$  quantifies the oscillations have established that neutrinos are massive to ΛCDM expectations when the inferred ΛCDM param- completely degenerate [103,104] lowever, their absolute SPT-3G 2-point CMB spectra drive the preference for eithter sum of the neutrino masses  $m_v > 60$  meV, for a ing effect is artificially removed:

A<sub>I</sub> ×A<sub>I</sub> <sup>φφ</sup> ¼ 1.11 0.11δPlank CMB þ SPT-3G lensÞ; A<sub>1</sub> ×A<sub>1</sub><sup>φφ</sup> ¼ 1.040.13 ŏSPT-3G CMB þ SPT-3G lens**Ø**30Þ

predicted by the best-fit \(\text{CDM}\) parameters as determined parameterand the expansion rate but not to the matter been marginalized over.

#### Neutrino mass

By being sensitive to matter clustering aintermediate redshifts and mostly linear scale MB lensing measurements can also provide insights on the neutrino sector

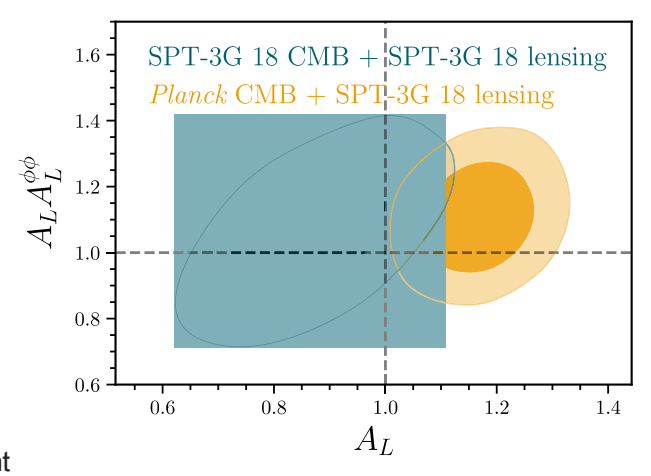
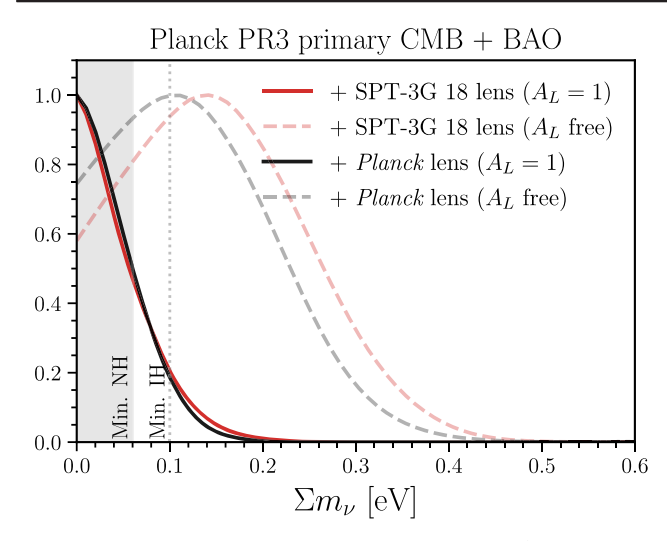


FIG. 11. Consistency check between direct and indirect CMB function and with ∧CDM predictions, we follow Calabreselensing measurements he amount of lensing directly inferred et al. [100] and Planck Collaboration et al. [34]. In additiorfrom SPT-3G data (Ακ Α<sup>φφ</sup><sub>L</sub>) is consistent with what is predicted by the best-fit ΛCDM cosmology as determined from primary scales the lensing power spectrum that affects both the lensing power spectrum that affects between the lens ที่dds for both Planck PR3 primary CMB (orange contours) as well as 2018 SPT-3G data (blue contours).

e.g., [8,101,102], one of the most elusive constituents of the lensing with either Planck or SPT-3G primary CMB anisotstandard model of particles. Observations of neutrino flavor overall amplitude of the measured lensing power with respecticles and that the three known mass eigenstates are not eters have been marginalized over the observed level of preaks scale is still unknown. The mass-squared differences smearing. As can be seen, while features in the Planck and easured in oscillation experiments put a lower bound on  $A_1 > 1$  or < 1, the amplitude of the lensing power spectrumormal hierarchy, or greater than 100 meV, for the inverted is consistent with both Planck and SPT-3G primary CMB hierarchy. While tritium beta decay end-point experiments ACDM predictions when the sensitivity to the peak smootlike KATRIN have put constraints on the effective electron antineutrino mass at the level of  $m_{v}$  < 800 meV (90% C.L., [105]), and are expected to improve by a factor of four, cosmological measurements already have a stronger (albeit model dependent) sensitivity and have the potential to make a mass measurement n the next decade or so The SPT-3G lensing reconstruction shows no evidence for an at low redshifts and contribute to both the matter density from primary CMB data when the peak smoothing effect has consequently, in a universe where neutrinos possess mass, clustering on scales below their free-streaming length. the growth of structures below the free-streaming length will be suppressed compared to a universe where neutrinos are massless.

In Fig. 12, we show the marginalized posterior on the sum of the neutrino masses in a ΛCDM b m, cosmology when combining primary CMB, BAO, and CMB lensing datasets(solid lines). When freeing follow the argument of Lesgourgues and Pastq6] and 0.3 on the amplitude of the foreground bias template, where the consider a degenerate combination of three equally massive dispersion is taken from the scatter in the template amplitudes beutrinos, as was done in the Planck papers [34]. The top panel shows the inclusion of Planck primary CMB data, while the bottom one shows the constraints obtained using

<sup>&</sup>lt;sup>15</sup>If we instead impose a less conservative Gaussian prior 1. 16 cutouts of the AGORA simulations as discussed in Set E, we find  $A_1^{\varphi\varphi} \frac{1}{4} 1.014 0.076$ .



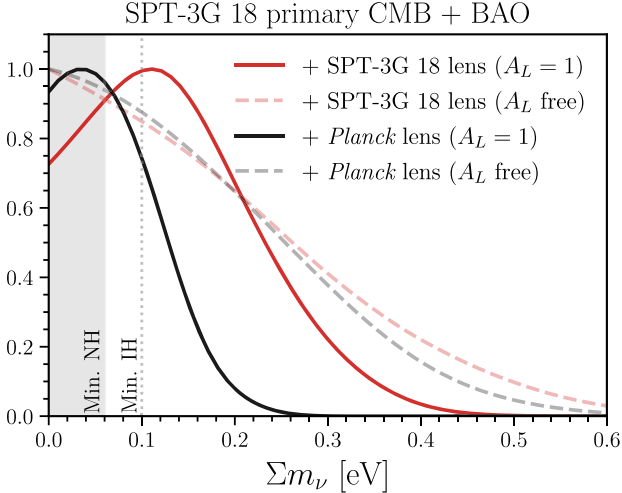


FIG. 12 Marginalized constraints on the sum of the neutrino masses  $m_v$  when BAO and either Planck (upper panel) or SPTmary CMB is about  $1\sigma$  low with respect to  $\Lambda$ CDM 3G (lower panel) CMB temperature and polarization power spectra are folded into the cosmological inference. In each panelle posteriors peak azero mass and broaden so thathe the red and black lines show the effect of including direct lensing constraints become m<sub>v</sub> < 0.45 eV (for SPT-3G lensing) corresponding light dashed lines show instead the constraint when we remove the lensing information in the primary CMB, i.e. we allow A to vary. The expectations for minimal masses based on oscillation measurements the normal (NH) and and the dotted verticalline, respectively.

SPT-3G CMB temperature and polarization spectra as oulargely driven by the lensing smoothing on the acoustic early Universe probe. In each panel, the red and black linesaks, which partially breaks the geometrical egeneracy denote respectively the addition of either SPT-3G or Planckoll. Therefore, a direct measurement of the lensing ing constraints in a ΛCDM b m, b A<sub>1</sub> cosmology,i.e. when we marginalize over the lensing information in the primary CMB (semitransparentlashed lines, same color coding as above).

The 95% C.L. constraint on the sum of the neutrino massesfrom Planck CMB b BAO is  $m_v < 0.13 \text{ eV}$ which remains

$$M_{v} < 0.13 \text{ eV}$$

ðPlanck CMB þ BAO þ SPT-3G lens; 2σÞ; ð31Þ

when SPT-3G lensing information is added. This constraint with SPT-3G lensing is similar to that with Planck lensing  $m_v < 0.11$  eV. While the inclusion of CMB lensing does not seem to improve or change the constraint significantly, we recall that the neutrino constraints based on Planck PR3 primary CMB are known to be artificially tight because of the anomalous lensing smoothing amplitude (see Sec.VI D 1). We therefore repeathe exercise when allowing A to vary. As expected, the  $2\sigma$  upper limits combined with SPT-36 and Planck lensing are relaxed to  $m_{v} < 0.32 \text{ eV}$  and  $m_v < 0.28 \text{ eV}$ , respectively.ln both casesthe posteriors peak at neutrino masses around m<sub>v</sub> around 0.1–0.2 eV.

To investigate the neutrino constraint sensitivity to primary CMB and potential lensing anomalies, we replace Planck PR3 primary CMB with the latest SPT-3G temperature and polarization power spectra. Although not as constraining as the Planck datase SPT-3G can provide a useful consistency checkA joint analysis of SPT-3G CMB b BAO reveals a 2σ constraint on the neutrino mass  $m_v < 0.43 \text{ eV}$ , which becomes

with the inclusion of SPT-3G lensingThe corresponding constraintusing Planck lensing is comparatively tighter,  $_{\rm P}$  m<sub>v</sub> < 0.17 eV. Both posteriors peak at values  $m_v > 0$ . The lensing parameter from SPT-3G priexpectations (see Fig11). When A is allowed to vary,  $m_v < 0.32 \text{ eV (for Planck lensing)}.$ 

# Curvature

CMB lensing measurements also allow us to testhe inverted (IH) hierarchies are denoted by the gray shaded band mean spatial curvature of the Universe, which is predicted to be close to flat in the majority of inflationary models. Curvature constraints from primary CMB spectra are lensing datasets. In addition we also show the correspondmplitude can further resolve the degeneracy and sharpen constraints on  $\Omega_k$ . Once again, Planck temperature and polarization anisotropies alone presents with a curious feature, showing a 2 – 3σ preference fomonflat models e.g., [34,109,110]. This is driven by the  $\mathbf{A}_{K}$  degeneracy and the presence of an enhanced lensing amplitude in the Planck 2018 data releaseThe preference for an egative curvature weakens in the analysis of Planck NPIPE

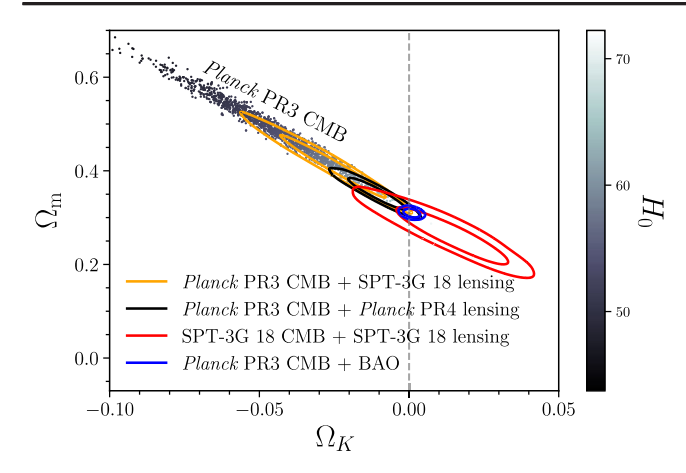


FIG. 13. Constraints on curvature and the matter density ing Hubble constantvalues. The orange and black solid lines show the constraints inferred by adding either SPT-3G or Planck lensing datasets, respectively. The blue solid lines denoted the solid instead the constraints from Planck primary CMB combined BAO data, and indicate consistency with a flageometry. The lensing are highlighted in red.

maps [98] and is not presentin either SPT [32] or ACT data [99]. Moreover, the addition of BAO data strongly breaks the geometric degeneracy and eliminates the pref-systematicuncertainty, stemming from beam and map erence for nonzero  $\Omega$ .

The geometrical degeneracy isclearly visible in the colored scatter points in Fig13, which show the allowed region in the  $\Omega_{\!K}\text{-}\Omega_{m}$  parameter space using only primary CMB information from Planck, for which we find  $-0.078 < \Omega_K < -0.010$  (95% C.L.). The inclusion of lensing information from SPT-3G shrinks the allowed 2σ region to

which is still ~2 $\sigma$  away from  $\Omega_K~1\!\!/_4~0.^{16}$  For comparison, when we instead include Planck lensing, the 2σ constraint logical parameter constraints With SPT-3G 2018 lensing becomes  $Q \frac{1}{4}$  -0.01  $\stackrel{\text{b0.012}}{\stackrel{\text{c}}{=}}$ . Using only SPT data for both

$$\Omega_{K}$$
 ¼ 0.0140.023ðSPT-3G CMB þ SPT-3G lens; 2σÞ;

ð34Þ

on the spatial curvature into a constrainton the cosmological constant density parameter  $\Omega^{1/4}$  1 –  $\Omega_{\rm m}$  –  $\Omega_{\rm K}$  as done in the first indirect evidence for dark energy using only CMB data [9]. Combining SPT-3G CMB lensing with either Planck or SPT-3G primary CMB, we obtain the following 1σ bounds:

 $\Omega_{\Lambda}$  ¼ 0.61 $\frac{20.035}{0.029}$ ðPlanck CMB þ SPT-3G lensÞ; 

Again, the constraint from Planck CMB and SPT-3G CMB lensing is shifted due to the anomalous peak smoothing in Planck.

## VII. CONCLUSIONS

We have presented the firstanalysis of CMB lensing parameter obtained from the analysis of Planck primary CMB, using data from SPT-3G, the current camera on the South with scattered points color-coded according to their correspond Pole Telescope. With the 95 GHz and 150 GHz temperature data from the SPT-3G 2018 datasetwe produced highwithouthern sky, with S=N ratio per mode greater than unity for modes at L ≤ 70 to 100 depending on the constraints obtained from both 2018 SPT-3G primary CMB and requency combination. We combined the cross-frequency convergencemaps and reported a minimum-variance CMB lensing power spectrum overthe multipole range  $50 \le L \le 2000$ . We constrained the lensing amplitude to be A<sup>MV</sup> ¼ 1.020 0.060, a 5.9% precision measurement. The calibration uncertainties, is 0.016, about 27% of the statistical uncertainty. When marginalizing over a foreground bias template, we found A1/4 1.063 0.090. We conducted a set of consistency checks and null tests on our results and found no evidence of significant bias in our measurement.

We have discussed the cosmological implications of the SPT-3G 2018 data lensing measurements within the ACDM model and in a number of 1- and 2-parameter extensionsOur lensing amplitude agrees with those from ACT and Planck with or without foreground marginalization. While foreground marginalization has minimal impact on cosmological constraints—foreground biasis small compared to the uncertainty—it is included for all cosmoalone, we constrained  $\alpha\Omega_{\rm m}^{0.25}$  to be 0.595 0.026—a primary CMB and lensing, the curvature is constrained to precision of 4.4%. This result is broadly consistent with other CMB lensing measurements, including previous SPT-SZ, SPTpol, ACT, and Planck results, as well as with Planck's primary CMB anisotropy measurements. When complementing this with BAO data from galaxy consistent with a flat universe. Finally, we can turn the limqurveys, we were able to constrain the matter density and structure amplitude parameters to  $\Omega_{\rm m} \ \% \ 0.320^{0.021}_{0.026}$ and σ<sub>8</sub> ¼ 0.810 0.033, consistentwith ΛCDM expectations based on Planck primary CMB. There is some tension between CMB and low-redshift measurements of H<sub>0</sub> and S<sub>8</sub>. When combined with BAO, our measurement is consistent with the cosmology inferred from

<sup>&</sup>lt;sup>16</sup>We note that in this run, the posterior of the inferred foreground contamination parameters tends to shift to the upper limit of the prior boundary.

Planck primary CMB measurements Specifically the parameter combination  $S_8$  ½  $\sigma_{\!\! 8}$   $\Omega_m$  =0.3 was determined by the combination  $S_8$  ½  $\sigma_{\!\! 8}$ mined to be 0.836 0.039, about 1.6–1.8 $\sigma$  higherthan the values inferred from optical surveys such as DES, HSC, and KiDS. The Hubble constant result of H<sub>0</sub> ¼ 68.8 hm s 1 Mpc 1 agrees with other early-Universe estimates and is approximately 2.6 or lower than estimates by the Kavli Institute of Cosmological Physics at the based on Cepheid-calibrated local distance ladder measurements.

spectrum of Planck, which is 2 – 3σ higher than whats expected from the ACDM model, has notable effects on estimates for cosmological parameters like  $\Sigma$  and  $\Omega_c$ . To isolate the impactfrom the excess smoothingwe either marginalized over A<sub>L</sub> when combining with Planck's primary spectrum or combined with primary spectrum measurements rom the SPT-3G 2018 data. First, we demonstrated that SPT-3G 2018 lensing amplitude is consistentwith the ACDM expectation when effects of CMB were marginalized over. In combination with the Planck and BAO datasetshe sum of neutrino masses is  $\Sigma m_v < 0.13 \text{ eV}$  and  $\Sigma m_v < 0.32 \text{ eV}$  (95% C.L.) without and with A marginalized overAlternatively, when using SPT-3G 2018 CMB data in place of Planckye obtained  $\Sigma m_v < 0.30 \text{ eV}$  (95% C. L.;  $\Lambda$  ¼ 1). Using primary CMB from Planck in combination with SPT-3G lensing drives a Advanced Research, and the Fonds de recherchedu  $2\sigma$  preference for a nonflat universe and favors a lower  $\Omega$ Québec Nature et technologies. The SLAC authors of 0.6130.059. The 2σ preference disappears when replacacknowledge support by the Department of Energy, ing the primary CMB from Planck with that from SPT-3G Contract No. DE-AC02-76SF00515. The UCLA and MSU surface acceptance from NOS ACT. 2018 data, yielding Q ¼ 0.01 $\stackrel{Q}{\leftarrow}_{0.026}^{0.023}$  (95% C. L.) and Q of 0.722 0.054

2018 observing season with a half-functioning focal plane Urbana, IL. K. F. acknowledges support from the resulting in higher per-year map noisenap depths using data from subsequent observing seasons are matching expectations[42]. Our lensing measurementis signal dominated up to L = 100; upcoming analyses using two years of data on the 1500 defigeld will expand the signaldominated region out to multipoles of a few hundred. resulting in a ≈2% measurement of the lensing amplitude 0186. J. V. acknowledges support from the At these low map noise levels, polarization measurement Foundation. W. L. K. W. is supported in part by the will contribute the majority of S=N ratios in future SPT-3GDepartment of Energy, Laboratory Directed Research lensing analyses, and employing optimal methods e.g., [111–113] will further this dataset's science readhighfidelity lensing maps generated by SPT-3G will be critical Laboratory, under Contract No. DE-AC02-76SF00515. in removing the lensing contamination in the search of primordial gravitational waves, parametrized by the tensor Open Science Grid [116,117] which is supported by the to-scalarratio r, when jointly analyzed with data from BICEP Array [114]. The most stringent constraint on r to date from [115] is already limited by lensing. With SPT-3G 's full-survey lensing mapye expect to improve BICEP Array's runcertainty by a factor of about 2.5, reaching σðrÞ of about 0.003.

#### ACKNOWLEDGMENTS

We would like to thank Mathew Madhavacheril and Frank Qu for clarifications regarding the ACT DR6 lensing analysis. The South Pole Telescope program is supported by the National Science Foundation (NSF)through the Grant No. OPP-1852617Partial support is also provided University of Chicago. Argonne National Laboratory's work was supported by the U.S.Department of Energy, The degree of peak smoothing in the temperature poweffice of High Energy Physics, under ContractNo. DE-AC02-06CH11357.Work at Fermi National Accelerator Laboratory, a DOE-OS, HEP User Facility managed by the Fermi ResearchAlliance, LLC, was supported under Contract No.DE-AC02-07CH11359. The Cardiff authors acknowledge support from the UK Science and Technologies Facilities Council (STFCThe IAP authors acknowledge supporfrom the Centre Nationald'Études Spatiales (CNES). This project has received funding from the European Research Council (ERC) under the European peak smoothing of either Planck or SPT-3G 2018 primary Union's Horizon 2020 research and innovation programme (Grant Agreement No. 101001897). The Melbourne authors acknowledge support from the Australian Research Council's Discovery Project scheme (No. DP210102386). The McGill authors acknowledge funding from the Natural Sciences and Engineering Research Council of Canada, Canadian Institute for MSU authors acknowledge support from NSF AST-1716965 and CSSI-1835865. M. A. and J. V. acknowledge support from the Center for AstroPhysic&urveys atthe While data for this analysis comes from only half of the National Center for Supercomputing Applications in Department of Energy Office of Science Graduate Student Research (SCGSR) Program.P.was supported by Laboratory Directed Research and Development (LDRD) funding from Argonne National Laboratory, provided by the Director, Office of Science, of the U.S. Department of Energy under Contract No. LDRD-2021and Developmentprogram and as part of the Panofsky Fellowship program at SLAC National Accelerator This research was done using resources provided by the NSF Award No. 1148698, and the U.S. Department of Energy's Office of Science. Some of the computing for this project was performed on the Sherlock cluster would like to thank Stanford University and the Stanford Research Computing Center for providing computational esources and support that contributed to these research results.

- [1] A. Lewis and A. Challinor, Weak gravitational lensing of the CMB, Phys.Rep. 429, 1 (2006).
- [2] F. Bianchini, W. L. K. Wu, P. A. R. Ade et al., Constraints on cosmologicalparameters from the 500 degSPTPOL lensing power spectrum Astrophys. J. 888, 119 (2020).
- [3] F. J.Qu, B. D. Sherwin, M. S. Madhavacheriet al., The atacamacosmology telescope: A measurement of the DR6 CMB lensing power spectrum and its implications for structure growth arXiv:2304.05202.
- [4] M. Kaplinghat, L. Knox, and Y.-S. Song, Determining neutrino mass from the cosmic microwave background alone, Phys. Rev. Lett. 91, 241301 (2003).
- [5] J. Lesgourgues, L. Perotto, S. Pastor, and M. Piat, Probing neutrino masses with CMB lensing extraction, Phys. Rev. D 73, 045021 (2006).
- [6] J. Lesgourguesand S. Pastor, Massive neutrinos and cosmologyPhys.Rep. 429, 307 (2006).
- [7] R. de Putter, O. Zahn, and E. V. Linder, CMB lensing constraints on neutrinos and dark energy, Phys. Rev. D 7922 J. Carron, M. Mirmelstein, and A. Lewis, CMB lensing 065033 (2009).
- [8] Z. Pan and L. Knox. Constraints on neutrino mass from cosmic microwave background and large-scale structure, [23] P. A. R.Ade, Y. Akiba et al. (POLARBEAR Collabora-Mon. Not. R. Astron. Soc. 454, 3200 (2015).
- [9] B. D. Sherwin, J. Dunkley, S. Das et al., Evidence for dark energy from the cosmic microwave background alone using the atacama cosmology telescope lensing measure-[24] M. Andr'es Osvaldo Aguilar Fa'undez, K. Arnold, C. ments, Phys. Rev. Lett. 107, 021302 (2011).
- [10] E. Calabrese, A. Cooray, M. Martinelli, A. Melchiorri, L. Pagano A. Slosar, and G. F. Smoot, CMB lensing constraints on dark energy and modified gravity scenarios, Phys.Rev.D 80, 103516 (2009).
- [11] T. Namikawa, F. R. Bouchet, and A. Taruya, CMB lensing bispectrum as a probe of modified gravity theories, Phys. Rev.D 98, 043530 (2018).
- [12] S. Singh, S. Alam, R. Mandelbaum, U. Seljak, S. Rodriguez-Torres, and S. Ho, Probing gravity with a joint analysis of galaxy and CMB lensing and SDSS spectroscopy, Mon. Not. R. Astron. Soc. 482, 785 (2018).
- [13] Y. Zhang, A. R. Pullen, S. Alam, S. Singh, E. Burtin, C.-H. Chuang, J. Hou, B. W. Lyke, A. D. Myers, R. Neveux, A. J. Ross, G. Rossi, and C. Zhao, Testing general relativity on [28] W. L. K. Wu, L. M. Mocanu, P. A. R. Ade et al., A cosmologicalscales atredshift z ~ 1.5 with quasar and CMB lensing, Mon. Not. R. Astron. Soc. 501, 1013 (2020).
- [14] S. Das, B. D. Sherwin, P. Aguirre et al., Detection of the power spectrum of cosmic microwave background lensing[29] M. Millea, C. M. Daley, T.-L. Chou et al., Optimal cosmic by the atacama cosmology telescope, Phys. Rev. Lett. 107, 021301 (2011).
- [15] B. D. Sherwin, A. van Engelen, N. Sehgalet al., Twoseason atacama cosmology telescope polarimeter lensing[30] Y. Omori, E. J. Baxter, C. Chang etal., Joint analysis of power spectrumPhys.Rev.D 95, 123529 (2017).
- [16] O. Darwish, M. S. Madhavacheril B. D. Sherwin et al., The atacama cosmology telescope: A CMB lensing mass map over 2100 square degrees of sky and its crosscorrelation with BOSS-CMASS galaxiesMon. Not. R. Astron. Soc. 500, 2250 (2020).
- [17] P. A. R. Ade et al. (BICEP2 Collaboration and Keck Array Collaboration), BICEP2/Keck Array VIII: Measurement of [32] L. Balkenhol, D. Dutcher, P. A. R. Ade et al., Constraints gravitational lensing from large-scale B-mode polarization, Astrophys.J. 833, 228 (2016).

- [18] P. A. R.Ade, Z. Ahmed, M. Amiri et al., BICEP/Keck. XVII. Line-of-sight distortion analysis: Estimates of gravitational lensing anisotropic cosmic birefringence atchy reionization, and systematic errors strophys. J. 949, 43 (2023).
- [19] P. A. R. Ade, N. Aghanim, C. Armitage-Caplan, M. Arnaud, M. Ashdown, F. Atrio-Barandela, J. Aumont, C. Baccigalupi, A. J. Banday et al. (Planck Collaboration), Planck 2013 results. XVII. Gravitational lensing by largescale structureAstron. Astrophys. 571, A17 (2014).
- [20] P. A. R.Ade, N. Aghanim, M. Arnaud, M. Ashdown, J. Aumont, C. Baccigalupi, A. J. Banday, R. B. Barreiro, J. G. Bartlett et al. (Planck Collaboration) Planck 2015 results. XV. Gravitational lensing, Astron. Astrophys. 594, A15 (2016).
- [21] N. Aghanim, Y. Akrami et al. (Planck Collaboration), Planck 2018 results. VIII. Gravitationallensing, Astron. Astrophys.641, A8 (2020).
  - from Planck PR4 maps, J. Cosmol. Astropart. Phys. 09 (2022) 039.
  - tion), Measurement of the cosmic microwave background polarization lensing powerspectrum with the POLAR-BEAR experiment Phys. Rev. Lett. 113, 021301 (2014).
  - Baccigalupi et al., Measurement of the cosmic microwave background polarization lensing power spectrum from two years of POLARBEAR data, Astrophys. J. 893, 85 (2020).
- [25] A. van Engelen, R. Keisler, O. Zahn et al., A measurement of gravitational lensing of the microwave background using south pole telescope data Astrophys. J. 756, 142 (2012).
- [26] K. T. Story, D. Hanson, P. A. R. Ade et al., A measurement of the cosmic microwave background gravitational lensing potential from 100 square degrees of SPTpol data, Astrophys.J. 810, 50 (2015).
- [27] Y. Omori, R. Chown, G. Simard et al., A 2500 deams lensing map from combined south pole telescope and Planck data Astrophys. J. 849, 124 (2017).
  - measurement f the cosmic microwave background lensing potential and power spectrum from 500 deg of SPTpol temperature and polarization datastrophys.J. 884, 70 (2019).
  - microwave background lensing reconstruction and parameter estimation with SPTpol data/strophys.J. 922, 259 (2021).
  - dark energy survey year 3 data and CMB lensing from SPT and Planck.I. Construction of CMB lensing maps and modeling choicesPhys.Rev.D 107, 023529 (2023).
- [31] D. Dutcher, L. Balkenhol, P. A. R. Ade et al., Measurements of the E -mode polarization and temperature-E mode correlation of the CMB from SPT-3G 2018 data, Phys.Rev.D 104, 022003 (2021).
  - on ΛCDM extensions from the SPT-3G 2018 E E and T E power spectraPhys.Rev.D 104, 083509 (2021).

- [33] L. Balkenhol, D. Dutcher, A. Spurio Mancini et al., Measurement f the CMB temperature powerspectrum and constraintson cosmology from the SPT-3G 2018 TT, TE, and EE dataset, Phys. Rev. D 108, 023510 (2023).
- [34] N. Aghanim, Y. Akrami et al. (Planck Collaboration), Planck 2018 results. VI. Cosmological parameters, Astron. Astrophys.641, A6 (2020).
- [35] W. L. Freedman, Measurements of the Hubble constant: Tensions in perspective strophys. J. 919, 16 (2021).
- [36] A. G. Riess, W. Yuan, L. M. Macri et al., A comprehensive measurement of the local value of the Hubble constant with 1 km s<sup>-1</sup> Mpc<sup>-1</sup> uncertainty from the Hubble space telescope and the SH0ES teamAstrophys.J. Lett. 934, L7 (2022).
- [37] Y. S. Murakami, A. G. Riess, B. E. Stahl, W. D. Kenworthy, D.-M. A. Pluck, A. Macoretta, D. Brout, D. O. Jones, D. M. Scolnic, and A. V. Filippenko, Leveraging SN la spectroscopicsimilarity to improve the measurement of ℍ arXiv:2306.00070.
- [38] M. Asgari, C.-A. Lin, B. Joachimi et al., KiDS-1000 cosmology: Cosmic shear constraints and comparison between two point statistics, Astron. Astrophys. 645, A104 (2021).
- [39] S. Joudaki, H. Hildebrandt, D. Traykova, N. E. Chisari, C. Heymans, A. Kannawadi, K. Kuijken, A. H. Wright, M. Asgari, T. Erben, H. Hoekstra, B. Joachimi, L. Miller, T. Tröster, and J. L. van den Busch, KiDS+VIKING-450 and DES-Y1 combined: Cosmology with cosmic shear, Astron. Astrophys. 638, L1 (2020).
- [40] T. M. C. Abbott, M. Aguena, A. Alarcon et al., Dark energy survey year3 results: Cosmologicalconstraints from galaxy clustering and weak lensingPhys. Rev. D 105, 023520 (2022).
- [41] J. E. Carlstrom, P. A. R. Ade, K. A. Aird et al., The 10 meter south pole telescope Publ. Astron. Soc. Pac. 123, 568 (2011).
- [42] J. A. Sobrin, A. J. Anderson, A. N. Bender et al., The J. Suppl. Ser. 258, 42 (2022).
- [43] R. Keisler, C. L.Reichardt, K. A. Aird et al., A measurement of the damping tail of the cosmic microwave background power spectrum with the south pole telescope, Astrophys.J. 743, 28 (2011).
- [44] Y. Hoffman and E. Ribak, Constrained realizationsof Gaussian fields—A simple algorithm strophys. J. Lett. 380, L5 (1991).
- [45] A. Benoit-Lévy, T. Déchelette, K. Benabed, J.-F. Cardoso, D. Hanson, and S. Prunet, Full-sky CMB lensing reconstruction in presence of sky-cuts, Astron. Astrophys. 555. A37 (2013).
- [46] S. Raghunathan, G. P. Holder, J. G. Bartlett, S. Patil, C. L. Reichardt, and N. Whitehorn, An inpainting approach to tackle the kinematic and thermalSZ induced biases in CMB-cluster lensing estimators, J. Cosmol. Astropart. Phys.11 (2019) 037.
- [47] L. E. Bleem, B. Stalder, T. de Haan et al., Galaxy clusters discovered via the Sunyaev-Zel'dovich effect in the 2500square-degree SPT-SZ survelystrophys.J. Suppl. Ser. 216, 27 (2015).

- [48] M. Lembo, G. Fabbian, J. Carron, and A. Lewis, CMB lensing reconstruction biases from masking extragalactic sources, Phys. Rev. D 106, 023525 (2022).
- [49] Planck Collaboration, Planck Legacy Archive (2018), https://www.cosmos.esa.int/web/planck/pla.
- [50] A. Lewis and A. Challinor, CAMB: Code for Anisotropies in the Microwave Background, Astrophysics Source Code Library (2011), record ascl:1102.026;ttp://ascl.net/1102
- [51] K. M. Górski, E. Hivon, A. J. Banday, B. D. Wandelt, F. K. Hansen, M. Reinecke, and M. Bartelmann, HEALPix: A framework for high-resolution discretization and fast analysis of data distributed on the spherestrophys.J. 622, 759 (2005).
- [52] A. Lewis, Lensed CMB simulation and parameter estimation, Phys.Rev.D 71, 083008 (2005).
- [53] C. L. Reichardt, S. Patil, P. A. R. Ade et al., An improved measurement the secondary cosmic microwave background anisotropies from the SPT-SZ + SPTpsulrveys, Astrophys.J. 908, 199 (2021).
- [54] M. P. Viero, L. Wang, M. Zemcov et al., HerMES: Cosmic infrared background anisotropiesand the clustering of dusty star-forming galaxies, Astrophys. J. 772, 77 (2013).
- [55] L. D. Shaw, D. Nagai, S. Bhattacharyaand E. T. Lau, Impact of cluster physics on the Sunyaev-Zel'dovich power spectrumAstrophys.J. 725, 1452 (2010).
- [56] L. D. Shaw, D. H. Rudd, and D. Nagai, Deconstructing the kinetic SZ power spectrum, Astrophys. J. 756, 15 (2012).
- [57] O. Zahn, C. L. Reichardt, L. Shaw et al., Cosmic microwave background constraints on the duration and timing of reionization from the south pole telescopastrophys.J. 756, 65 (2012).
- [58] A. van Engelen, S. Bhattacharya, N. Sehgal, G. P. Holder, O. Zahn, and D. Nagai, CMB lensing power spectrum biases from galaxies and clusters using high-angular resolution temperature maps, Astrophys. J. 786, 13 (2014).
- [59] Y. Omori, AGORA: Multi-component simulation for crosssurvey sciencearXiv:2212.07420.
- design and integrated performance of SPT-3G, Astrophys [60] W. B. Everett, L. Zhang, T. M. Crawford et al., Millimeterwave point sources from the 2500 square degree SPT-SZ survey: Catalog and population statistics. Astrophys. J. 900, 55 (2020).
  - [61] A. Cavaliere and R.Fusco-FemianoThe distribution of hot gas in clusters of galaxies, Astron. Astrophys. 70, 677 (1978).
  - [62] W. Hu and T. Okamoto, Mass reconstruction with cosmic microwave background polarization Astrophys. J. 574, 566 (2002).
  - [63] G. Fabbian, A. Lewis, and D. Beck, CMB lensing reconstruction biases in cross-correlation with large-scale structure probes J. Cosmol. Astropart. Phys. 10 (2019)
  - [64] T. Namikawa, D. Hanson, and R. Takahashi, Biashardened CMB lensingMon. Not. R. Astron. Soc. 431, 609 (2013).
  - [65] L. M. Mocanu, T. M. Crawford, K. Aylor et al., Consistency of cosmic microwave background temperature measurements in three frequency bands in the 2500square-degree SPT-SZ survey, J. Cosmol. Astropart. Phys. 07 (2019) 038.

- [66] N. Aghanim, M. Arnaud, M. Ashdown, J. Aumont, C. Baccigalupi, A. J. Banday, R. B. Barreiro, J. G. Bartlett, N. Bartolo et al. (Planck Collaboration), Planck 2015 results. XI. CMB power spectra, likelihoods, and robustness of parameters Astron. Astrophys. 594, A11 (2016).
- [67] O. J. Dunn, Multiple comparisons among mean&merican Statistical Association 562 (1961).
- [68] T. Namikawa, D. Yamauchi, and A. Taruya, Full-sky lensing reconstruction of gradient and curl modes from CMB maps, J. Cosmol. Astropart. Phys. 01 (2012) 007.
- [69] M. Robertson and A. Lewis, How to detect lensing rotation, J. Cosmol. Astropart. Phys. 08 (2023) 048.
- [70] P. Peebles, The Large Scale Structure of the Universe (Princeton University Pressrinceton, NJ, 1980).
- [71] A. J. Mead, T. Tröster, C. Heymans, L. Van Waerbeke, and I. G. McCarthy, A hydrodynamical halo model for weaklensing cross correlation Astron. Astrophys. 641, A130 (2020).
- [72] M. S. MadhavacherilF. J.Qu, B. D. Sherwin et al., The atacama cosmology telescop@R6 gravitationallensing map and cosmological arameters ar Xiv: 2304.05203.
- [73] M. M. Schmittfull, A. Challinor, D. Hanson, and A. Lewis, Joint analysis of CMB temperature and lensingreconstruction powespectra, Phys. Rev. D 88, 063012 (2013).
- [74] P. Motloch, W. Hu, and A. Benoiteký, CMB lens sample covariance and consistency relation hys. Rev. D 95, 043518 (2017).
- [75] J. Peloton, M. Schmittfull, A. Lewis, J. Carron, and O. Zahn, Full covariance of CMB and lensing reconstruction [91] A. Amon, D. Gruen, M. A. Troxel et al., Dark energy power spectraPhys.Rev.D 95, 043508 (2017).
- [76] C. Trendafilova, The impact of cross-covariancesetween the CMB and reconstructed lensing power, J. Cosmol.Astropart.Phys.10 (2023) 071.
- [77] J. Hartlap, P. Simon, and P. Schneider, Why your model parameter confidences migbe too optimistic. Unbiased estimation of the inverse covariance matrix, Astron. Astrophys.464, 399 (2007).
- [78] G. Simard, Y. Omori, K. Aylor et al., Constraintson cosmological parameters from the angular power spectrum lensing map Astrophys. J. 860, 137 (2018).
- [79] S. Alam, M. Ata, S. Bailey et al., The clustering of galaxies in the completed SDSS-III baryon oscillation spectroscopic survey: Cosmological analysis of the DR12 galaxy sample, Mon. Not. R. Astron. Soc. 470, 2617 (2017).
- [80] A. J. Ross, L. Samushia, C. Howlett, W. J. Percival, A. Burden, and M. Manera, The clustering of the SDSS DR7 main Galaxy sample—I. A 4 per cent distance measure at [97] P. Lemos and A. Lewis, CMB constraints on the early z ¼ 0.15, Mon. Not. R. Astron. Soc. 449, 835 (2015).
- [81] F. Beutler, C. Blake, M. Colless, D. H. Jones, L. Staveley-Smith, L. Campbell, Q. Parker, W. Saunders, and F. Watson, The 6dF galaxy survey: Baryon acoustic oscillations and the local Hubble constant, Mon. Not. R. Astron. Soc. 416, 3017 (2011).
- [82] S. Alam, M. Aubert, S. Avila et al., Completed SDSS-IV extended baryon oscillation spectroscopic survey: Cosmological implications from two decades of spectroscopic surveys at the apache point observatory, Phys. Rev. D 103, 083533 (2021).

- [83] N. Aghanim, Y. Akrami et al. (Planck Collaboration), Planck 2018 results. V. CMB power spectra and likelihoods, Astron. Astrophys. 641, A5 (2020).
- [84] R. J. Cooke, M. Pettini, and C. C. Steidel, One percent determination of the primordial deuterium abundance, Astrophys.J. 855, 102 (2018).
- [85] V. Mossa, K. Stöckel, F. Cavanna et al., The baryon density of the Universe from an improved rate of deuterium burning, Nature (London) 587210 (2020).
- [86] Z. Pan, L. Knox, and M. White, Dependence of the cosmic microwave background lensing powespectrum on the matter density, Mon. Not. R. Astron. Soc. 445, 2941 (2014).
- [87] E. J. Baxter and B. D. Sherwin, Determining the Hubble constantwithout the sound horizon scaleMeasurements from CMB lensing, Mon. Not. R. Astron. Soc. 501, 1823 (2021).
- [88] W. L. Freedman B. F. Madore, D. Hatt, T. J. Hoyt, I.-S. Jang, R. L. Beaton, C. R. Burns, M. G. Lee, A. J. Monson, J. R. Neeley, M. M. Phillips, J. A. Rich, and M. Seibert, The Carnegie-Chicago Hubble program/III. An independent determination of the Hubble constant based on the tip of the red giant branchAstrophys.J. 882, 34 (2019).
- [89] W. L. K. Wu, P. Motloch, W. Hu, and M. Raveri, Hubble constant difference between CMB lensing and BAO measurementshys.Rev.D 102, 023510 (2020).
- [90] E. Abdalla et al. Cosmology intertwined: A review of the particle physics astrophysics and cosmology associated with the cosmological tensions and anomalies.J. High Energy Astrophys34, 49 (2022).
- survey year 3 results: Cosmology from cosmic shear and robustness to data calibratio hys. Rev. D 105, 023514 (2022).
- [92] L. F. Secco, S. Samuroff, E. Krause et al., Dark energy survey year 3 results: Cosmology from cosmic shear and robustness to modeling uncertainty Phys. Rev. D 105, 023515 (2022).
- [93] X. Li, T. Zhang, S. Sugiyama etal., Hyper suprime-cam year 3 results: Cosmology from cosmic shear two-point correlation functionsarXiv:2304.00702.
- of a combined 2500 de SPT-SZ and Planck gravitational [94] R. Dalal, X. Li, A. Nicola et al., Hyper suprime-cam year 3 results: Cosmology from cosmic shear power spectra, arXiv:2304.00701.
  - [95] T. M. C. Abbott et al., DES Y3 + KiDS-1000: Consistent cosmology combining cosmic shear surveys, Open J. Astrophys.6, 2305.(2023).
  - [96] P. Motloch and W. Hu, Lensinglike tensions in the Planck legacy release, hys. Rev. D 101, 083515 (2020).
    - Universe independent of late-time cosmologhys. Rev. D 107, 103505 (2023).
  - [98] E. Rosenberg, S. Gratton, and G. Efstathiou, CMB power spectra and cosmological parameters from Planck PR4 with CamSpec, Mon. Not. R. Astron. Soc. 517, 4620 (2022).
  - [99] S. Aiola, E. Calabrese L. Maurin et al., The atacama cosmology telescope: DR4 maps and cosmological parameters, J. Cosmol. Astropart. Phys. 12 (2020) 047.
  - [100] E. Calabrese, A. Slosar, A. Melchiorri, G. F. Smoot, and O. Zahn, Cosmic microwave weak lensing data as a test the dark universePhys.Rev.D 77, 123531 (2008).

- [101] K. M. Smith, A. Cooray, S. Das, O. Doré, D. Hanson, C. Hirata, M. Kaplinghat, B. Keating, M. Loverde, N. Miller, G. Rocha, M. Shimon, and O. Zahn, Gravitational lensing[110] E. Di Valentino, A. Melchiorri, and J. Silk, Planck in American Institute of Physics Conference Series, Vol. 1141, American Institute of Physics Conference Series (2009)pp. 121–178,10.1063/1.3160886.
- [102] K. N. Abazajian, K. Arnold, J. Austermann et al., Neutrino physics from the cosmic microwave background and large scale structureAstropart.Phys.63, 66 (2015).
- [103] Y. Fukuda, T. Hayakawa, E. Ichihara et al., Evidence for oscillation of atmospheric neutrino®, hys. Rev. Lett. 81, 1562 (1998).
- [104] Q. R. Ahmad, R. C. Allen, T. C. Andersen etal., Direct evidence for neutrino flavor transformation from neutralcurrent interactions in the sudbury neutrino observatory, [114] H. Hui, P. A. R.Ade, Z. Ahmed et al., BICEP array: A Phys.Rev.Lett. 89, 011301 (2002).
- [105] M. Aker et al., Direct neutrino-mass measuremewith sub-electronvolt sensitivity at. Phys. 18, 160 (2022).
- [106] K. Abazajian, G. Addison, P. Adshead, Z. Ahmed, S. W. Allen, D. Alonso, M. Alvarez, A. Anderson, K. S. Arnold, [115] P. A. RAde, Z. Ahmed, M. Amiri et al., Improved con-C. Baccigalupiet al. (CMB-S4 Collaboration), CMB-S4 science casereference designand project plan, arXiv: 1907.04473.
- [107] M. Gerbino, E. Grohs, M. Lattanzi et al., Synergy betwee [116] R. Pordes et al., The open science grid, J. Phys. Conf. Ser. cosmological and laboratory searches in neutrino physics, Phys. Dark Universe 42,101333 (2023).
- [108] R. Stompor and G. Efstathiou, Gravitational lensing of cosmic microwave background anisotropies and cosmological parameter estimationMon. Not. R. Astron. Soc. 302, 735 (1999).

- [109] W. Handley, Curvature tension: Evidence for a closed universe, Phys. Rev. D 103, L041301 (2021).
- evidence for a closed Universe and a possible crisis for cosmology, Nat. Astron. 4, 196 (2019).
- [111] M. Millea and U. c. v. Seljak, Marginal unbiased score expansion and application to CMB lensinghys. Rev. D 105, 103531 (2022).
- [112] L. Legrand and J. Carron, Lensing power spectrum of the cosmic microwave background with deep polarization experimentsPhys.Rev.D 105, 123519 (2022).
- [113] F. Bianchini and M. Millea, Inference of gravitational lensing and patchy reionization with future CMB data, Phys.Rev.D 107, 043521 (2023).
- multi-frequency degree-scale CMB polarimetain Proceedings of SPIE, Vol. 10708, Society of Photo-Optical Instrumentation Engineers (SPIE) Conference Series (2018), p. 1070807, 10.1117/12.2311725.
- straints on primordial gravitational waves using Planck, WMAP, and BICEP/Keck observations through the 2018 observing season, Phys. Rev. Lett. 127, 151301 (2021).
  - 78, 012057 (2007).
- [117] I. Sfiligoi, D. C. Bradley, B. Holzman, P. Mhashilkar, S. Padhi, and F. Wurthwein, The pilot way to grid resources using glideinWMS, in 2009 WRI World Congress on Computer Science and Information Engineering (2009), Vol. 2, pp. 428-432,10.1109/CSIE.2009.950.